Temperatures recorded by cosmogenic noble gases since the last glacial maximum in the Maritime Alps

Marissa M. Tremblay[1,2,*], David L. Shuster[1,2], Matteo Spagnolo[3], Hans Renssen[4], Adriano Ribolini[5]

[1]Department of Earth and Planetary Science, University of California, Berkeley, Berkeley, CA, 94720-4767 USA

[2]Berkeley Geochronology Center, Berkeley, CA, 94709, USA

[3]Department of Geography and Environment, School of Geosciences, University of Aberdeen, Aberdeen, AB24 3UF, UK

[4]Department of Natural Sciences and Environmental Health, University College of Southeast Norway, 3800 Bø, Norway

[5]Dipartimento di Scienze della Terra, Universita' di Pisa, 56126 Italy.

[*]Now located at Scottish Universities Environmental Research Centre, Rankine Avenue, East Kilbride, G75 0QF, UK

Correspondence to: Marissa M. Tremblay (marissa.tremblay@glasgow.ac.uk)

ABSTRACT

While proxy records have been used to reconstruct late Quaternary climate parameters throughout the European Alps, our knowledge of deglacial climate conditions in the Maritime Alps is limited. Here, we report temperatures recorded by a new and independent geochemical technique–cosmogenic noble gas paleothermometry–in the Maritime Alps since the last glacial maximum (LGM). We measured cosmogenic ^{3}He in quartz from boulders in nested moraines in the Gesso Valley, Italy. Paired with cosmogenic ^{10}Be measurements and ^{3}He diffusion experiments on quartz from the same boulders, the cosmogenic ^{3}He abundances record the temperatures these boulders experienced during their exposure. We calculate effective diffusion temperatures (EDTs) over the last ~22 ka ranging from 8 to 25ºC. These EDTs, which are functionally related to, but greater than, mean ambient temperatures, are consistent with temperatures inferred from other proxies in nearby Alpine regions and those predicted by a transient general circulation model. In detail, however, we also find different EDTs for boulders from the same moraines, thus limiting our ability to interpret these temperatures. We explore possible causes for these intra-moraine discrepancies including variations in radiative heating, our treatment of complex helium diffusion, uncertainties in our grain size analyses, and unaccounted for erosion or cosmogenic inheritance.

KEYWORDS

cosmogenic isotopes; paleoclimate; Quaternary; Europe

INTRODUCTION

Data from paleoclimate proxies constrain the dynamics of Earth's climate system on timescales inaccessible with the instrumental record. Proxy observations from key intervals of Earth's past climate, such as the last glacial maximum (LGM) and subsequent deglaciation, allow us to understand how the climate system responds to a change in forcing (e.g., Schmittner et al., 2011; Annan and Hargreaves, 2013; von der Heydt et al., 2016) and evaluate the ability of climate models to simulate the climate system's response (e.g., Schmidt et al., 2014; Annan and Hargreaves, 2015; Harrison et al., 2015) both of which improve our ability to forecast future climate change (e.g., Masson-Delmotte et al., 2013). Terrestrial proxies are particularly important for assessing how changes in large scale ocean-atmosphere dynamics manifest at a regional scale in the continental settings that people inhabit and depend upon.

An extensive network of terrestrial climate reconstructions since the last glacial maximum (LGM) exists across the European Alps from pollen, chironomids (midges), organic biomarkers, and inorganic isotope systems (e.g., Bartlein et al., 2011; Blaga et al., 2013; Heiri et al., 2014; Luetscher et al., 2015; Mauri et al., 2015). Despite such an extensive proxy network, our knowledge of deglacial climate conditions in the southern sector of the French and Italian Alps (hereafter referred to as the Maritime Alps) from proxy records is limited. Over the historical period, the Maritime Alps have been characterized by warmer mean annual temperatures (MAT),

63 smaller annual temperature amplitudes, lower mean annual precipitation (MAP), and snow cover
64 that is thinner and lasts for a smaller fraction of the year than in other Alpine sectors (Durand et
65 al., 2009a, 2009b). The Maritime Alps most likely remained the warmest Alpine sector during the
66 late Quaternary, given that the Maritime Alps are ~6º south of the northernmost eastern Alps, and
67 thus would have experienced greater insolation and generally higher temperatures. Warmer overall
68 conditions are consistent with species distribution and phylogeographical models, which suggest
69 that the Maritime Alps remained warmer than other parts of the Alps and functioned as a refugium
70 for plant species during the last glacial period (Casazza et al., 2016). Pollen-based climate
71 reconstructions from four high-elevation sites in the Maritime Alps suggest trends in temperature
72 and precipitation anomalies since the LGM that are broadly similar to those of other Alpine regions
73 (Ortu et al., 2008). However, these reconstructions are limited by nontrivial variations among the
74 four sites, likely due a combination of nonlocal pollen transport, limited modern analogues at high
75 elevations, and local effects on vegetation cover (Ortu et al., 2006; Ortu et al., 2008). There is one
76 reconstruction of mean July temperatures from fossil assemblages of chironomids proximal to the
77 Maritime Alps from Lago Piccolo di Avigliana ~90 km away, but this record is temporally limited
78 to 14–9.5 thousand years ago (Larocque and Finsinger, 2008). There are two additional proxy
79 studies from the Maritime Alps that extend into the latest Pleistocene which we are aware of: one
80 reporting fossil pollen assemblages in sixteen high elevation (> 1700 m) lakes (Brisset et al., 2015)
81 and one reporting fossil chironomid assemblages from Lac Long Inférieur in France (Gandouin
82 and Franquet, 2002). Neither of these studies interprets the proxies in terms of quantitative climate
83 parameters.

Due to the Maritime Alps' (1) southerly latitude, (2) generally lower elevations, and (3) proximity to the Mediterranean Sea, the late Quaternary climatic evolution and glacier dynamics in this region may have differed substantially from those in Alpine regions further north and inland (e.g., Kuhlemann et al., 2008), despite the apparent synchronicity of glacier advances during the LGM and later stadials recorded by moraines across the Alps (e.g., Ivy-Ochs et al., 2007; Kuhlemann et al., 2008; Federici et al., 2017; Monegato et al., 2017). Reconstructing temperatures in the Maritime Alps since the LGM would therefore fill a gap in an otherwise extensive network of proxy-based reconstructions of post-LGM climate across the Alps, and address the specific question of how climate evolution in the Maritime Alps during deglaciation may have differed from other Alpine sectors. For example, in combination with the positions and chronology of moraines, a well-resolved local temperature record could be used to inform a simple glacier mass balance model for valleys in the Maritime Alps during the deglacial period. With constraints on local deglacial temperatures, a mass balance model could be used to crudely invert for changes in precipitation during deglaciation (e.g., Kessler et al., 2006). This paired temperature-precipitation reconstruction could then be compared to proxy records further north and inland in the Alps to assess how climate and glacier dynamics varied across the region during deglaciation (e.g., Becker et al., 2016).

In addition to assessing climatic variability during deglaciation across the European Alps, temperature records from an independent proxy could provide tests of different methodologies for

105 reconstructing climate parameters over this time interval. Reconstructions of climate parameters
106 from existing proxies in the European Alps commonly exhibit significant disagreement with
107 climate model simulations prior to the Holocene. Pollen-based reconstructions suggest much
108 colder temperatures, particularly in the winter, than the models predict (e.g., Jost et al., 2005),
109 while models predict higher summertime temperatures than chironomid-based reconstructions
110 during interstadials (Heiri et al., 2014). It is unclear whether these disagreements are attributable
111 to limitations in the global climate models used to simulate paleoclimate, a breakdown in the
112 assumptions of biologically-based reconstructions, or some combination of both. Having
113 independent pre-Holocene temperature records in the European Alps that are mechanistically
114 governed by different processes would therefore help in assessing the cause of the current proxy-
115 model discrepancies.
116
117 Cosmogenic noble gas paleothermometry is a new geochemical technique for reconstructing past
118 Earth surface temperatures (Tremblay et al., 2014a). Cosmogenic nuclides are produced by nuclear
119 interactions between target atoms and high-energy cosmic-ray particles, both in Earth's
120 atmosphere and in the solid Earth. Because the flux of secondary cosmic-ray particles decreases
121 exponentially with depth in rock, production of cosmogenic nuclides is restricted to the uppermost
122 few meters of the Earth's crust. The near surface production of rare nuclides such as ^{10}Be and ^{26}Al
123 by cosmic-ray particle interactions in common rock-forming minerals like quartz has been
124 extensively developed and utilized over the last 25 years by the geomorphology community to date
125 the surface exposure of rocks and quantify erosion rates (e.g., Granger et al., 2013). Rare noble

126 gas nuclides such as ^{3}He and ^{21}Ne are also produced in minerals by cosmic-ray particle
127 interactions. In common minerals like quartz and feldspars, these noble gases sometimes exhibit
128 diffusive loss at Earth surface temperatures (Shuster and Farley, 2005; Gourbet et al., 2012;
129 Tremblay et al., 2014b, 2017) and thus have not been widely utilized in cosmogenic nuclide
130 studies. However, cosmogenic noble gas–mineral pairs exhibiting open-system behavior
131 (simultaneous production and diffusion) can be utilized to reconstruct the temperatures that rocks
132 experience while exposed to cosmic-ray particles at Earth's surface when paired with observations
133 of a quantitatively retained cosmogenic nuclide. In high latitude and/or high altitude environments,
134 theoretical calculations indicate that measurements of ^{3}He in quartz can record temperature
135 variations from the last glacial period to the present (Tremblay et al., 2014a).
136
137 Here, we apply cosmogenic noble gas paleothermometry to investigate temperatures recorded by
138 cosmogenic noble gases since the LGM in the Gesso Valley, located in the southernmost Maritime
139 Alps of Italy approximately 40 km from the Gulf of Genoa in the Mediterranean Sea (Fig. 1). The
140 Gesso Valley was glaciated during the last glacial period. Glacial moraines and other geomorphic
141 features have been mapped throughout the basin (Federici et al., 2003), and cosmogenic ^{10}Be
142 exposure ages have been determined for boulders from three nested moraines that span from the
143 LGM to the Younger Dryas cold period (YD) (Federici et al., 2008, 2012, 2017). A number of
144 younger, Holocene-age moraines are preserved at higher elevations in the Gesso Valley (Fig. 1),
145 and small glaciers restricted to the highest elevation cirques persist today (Federici et al., 2017).
146 We measured cosmogenic ^{3}He abundances in quartz from a subset of the boulders with ^{10}Be

147 exposure ages from the three previously-studied moraines. We also conducted stepwise degassing
148 experiments to quantify the kinetics of ^{3}He diffusion in quartz from these boulders. Because
149 cosmogenic ^{3}He is simultaneously produced and diffusively lost during exposure in the moraines,
150 the 'apparent' exposure ages we calculate from the measured ^{3}He abundances are younger than
151 the 'true' exposure age determined from the ^{10}Be measurements. The difference between the
152 'apparent' and 'true' exposure ages can be used to calculate the integrated effective diffusion
153 temperature (EDT) during exposure. This integrated EDT is the temperature corresponding to the
154 mean diffusivity over a variable temperature history, and is therefore a function of the ambient
155 temperature history (Tremblay et al., 2014a). Paired with sample-specific ^{3}He diffusion kinetics,
156 we use the difference between 'apparent' and 'true' exposure ages to model the permissible
157 integrated EDTs, and by relation temperature histories, of each boulder. The presence of numerous
158 moraines with different exposure ages within the same valley is advantageous because it allows us
159 to obtain temperature records over different time intervals for an area with a shared climate history.
160

161 **METHODS**

162 Of the Gesso Valley boulders for which ^{10}Be measurements exist, we obtained archived material
163 (either whole rock or crushed, sieved fractions) from five samples for cosmogenic ^{3}He
164 measurements: one from the Piano del Praiet moraine (PDP10), two from the Ponte Murato
165 moraine (PM1, and PM4), and two from the Tetti del Bandito moraine (TDB1 and TDB3; Fig. 1
166 and Table 1). The ^{10}Be concentration in quartz for PDP10 ($223.8 \pm 9.6 \times 10^{3}$ atoms/g, using the
167 ^{10}Be/^{9}Be of Nishiizumi et al. (2007) for NIST SRM4325) was measured at the Scottish Universities

168 Environmental Research Centre Cosmogenic Isotope Analysis Facility in 2013; all other ^{10}Be
169 concentrations are previously published (Federici et al., 2008, 2012). The ^{10}Be exposure ages of
170 these boulders and other boulders from the same moraines have been used to associate the Piano
171 del Praiet, Ponte Murato, and Tetti del Bandito moraines with the Younger Dryas cold period, an
172 intermediate cold period referred to locally as the Bühl stadial at ~18 ka, and the LGM respectively
173 (Federici et al., 2008, 2012). We separated quartz from other phases using standard crushing,
174 sieving, and magnetic methods, followed by a 'frothing' technique commonly used in the ceramics
175 industry to separate quartz from feldspars in the largest sieve fraction that lacked composite grains
176 (Buckenham and Rogers, 1954). Purified quartz was then used to both measure cosmogenic ^{3}He
177 abundances and determine sample-specific ^{3}He diffusion kinetics. All helium isotope
178 measurements were made with an MAP 215-50 sector field mass spectrometer in the BGC Noble
179 Gas Thermochronometry Lab. Gas purification techniques and mass spectrometer analyses are as
180 described in Tremblay et al. (2014b).
181
182 For cosmogenic ^{3}He measurements, 100–500 mg aliquots of quartz were weighed and packed into
183 tantalum metal cups with both ends crimped, placed under vacuum in a sample chamber, and
184 heated with a feedback-controlled 150 W diode laser to either 500, 800, or 1100 ºC for 15 minutes
185 until subsequent extractions yielded He signals indistinguishable from the instrumental detection
186 limit. Empty tantalum cup blanks, heated to the same temperatures as the samples, and room
187 temperature procedural blanks were measured throughout each analytical session and subtracted
188 from the sample measurements; ^{3}He blank corrections were typically 2–3 x 10^{4} atoms. Aliquots of

189 air and ^{3}He-spiked helium standards of different manometrically-calibrated pipette volumes were
190 analyzed throughout an instrumental tuning period and used to determine helium sensitivities;
191 sensitivities varied linearly over the pressure range of the sample analyses, estimated by the size
192 of the ^{4}He signal. We propagated uncertainties from the blank corrections and sensitivity
193 regression into the cosmogenic ^{3}He concentrations. We assume that all ^{3}He is cosmogenic, as any
194 magmatic ^{3}He present at the time of mineral formation or nucleogenic ^{3}He (from the reaction ^{6}Li(n,
195 α)^{3}H) produced before reaching the near-surface is expected to be lost by diffusion (e.g., Tremblay
196 et al., 2014b), and any nucleogenic ^{3}He produced at the surface temperatures will likely be
197 negligible compared to cosmogenic ^{3}He (Lal, 1987).
198
199 To determine sample-specific diffusion kinetics, we conducted stepwise degassing experiments on
200 a proton-irradiated quartz grain from each sample. Proton irradiation generates a uniform
201 distribution of ^{3}He in quartz through similar nuclear reactions to those induced by cosmic ray
202 particles but with ten orders of magnitude or higher production rates, enabling step degassing
203 diffusion experiments to be conducted on single irradiated quartz grains (Shuster et al., 2004;
204 Shuster and Farley, 2005; Tremblay et al., 2014b). We conduct experiments on single grains rather
205 than multi-grain aliquots because it allows us to rapidly achieve and then maintain a spatially
206 homogeneous set point temperature, a critical requirement for step degassing experiments.
207 Previous work (Tremblay et al., 2014b) demonstrates that these single grain experiments are
208 reproducible for different quartz grains from the same sample. Quartz aliquots were irradiated with
209 a 228.5 MeV proton beam for 6 hours at the Francis H. Burr Proton Therapy Center at the

Massachusetts General Hospital in December 2015; the total proton fluence for this irradiation was 9.14 x 10^{15} p/cm^2. The irradiation target design and setup are detailed in Tremblay et al. (2017). Proton irradiated quartz aliquots were examined with a binocular microscope, and single crystals lacking visible penetrative fractures and inclusions (fluid or mineral) were selected for stepwise degassing. The dimensions of the chosen grains were measured to estimate the spherical equivalent radius used in later calculations to scale the diffusion lengthscale. Details of the stepwise degassing setup and helium measurements are described in Tremblay et al. (2014b).

In addition to determining the spherical equivalent radius of the quartz grains used in diffusion experiments, we also determined the spherical equivalent radii of the quartz grains used for cosmogenic measurements and assessed whether these radii are representative of the quartz size distribution in whole rock. Such an assessment is important because if we significantly reduced the grain size of quartz during the crushing process, this could lead to both an underestimation of the diffusion lengthscale to which the diffusion experiment size is scaled and missing cosmogenic ^{3}He from our measurements. First, we photographed and measured the dimensions of at least 100 quartz grains from the sieve fraction of each sample used for cosmogenic ^{3}He measurements. We determined major, intermediate, and minor axes of best fitting ellipsoids using the software ImageJ (Schneider et al., 2012) and calculated the radius of a sphere with the same surface area to volume ratio for each grain. We compared the spherical equivalent radii calculated using this approach to spherical equivalent radii determined from micro x-ray computed tomography (CT) analyses on a smaller number of grains from the same samples, wherein the grains were mapped in three

231 dimensions with a resolution better than 5 micrometers. CT scans were obtained on the Xradia
232 MicroXCT scanner at the University of Texas at Austin High-Resolution X-ray CT Facility and
233 processed using the software Blob3D (Ketcham, 2005) as described in Tremblay et al. (2017). This
234 comparison demonstrates that the ellipsoid approach consistently overestimates the spherical
235 equivalent radius by ~50%, likely because the ellipsoid method significantly underestimates the
236 surface area of grains. We therefore scaled the spherical equivalent radii from loose grain
237 measurements by a factor 1.5; the distribution of grain sizes from these measurements are shown
238 in Fig. 2. Also shown in Fig. 2 is the probability distribution of spherical equivalent radii of quartz
239 grains in whole rock. To determine this distribution, we determined circular equivalent radii from
240 measured sectional areas of at least 100 quartz grains in thin sections, and inverted the distribution
241 of circular equivalent radii to a distribution of spherical equivalent radii using the code
242 STRIPSTAR and the methodology described by Heilbronner and Barrett (2013). For PDP10, the
243 thin section was made from the same sample as the sample crushed for cosmogenic ^{3}He
244 measurements. For the PM and TDB moraines, no whole rock material from the original samples
245 was preserved; we therefore collected additional material from boulders exposed atop each of these
246 moraines for thin sections, and assume that the grain size observed in these samples is
247 representative of the samples for which we have cosmogenic ^{3}He data.
248
249 For all samples, the distribution of spherical equivalent radii for the sieve fraction has a smaller
250 standard deviation than the radii determined from thin section measurements (Fig. 2), which is not
251 surprising given that the sieving process removes larger and smaller grains. With the exception of

252 the PM samples, we find that the mean spherical equivalent radius of quartz in the sieve fraction
253 is equal to or slightly greater than the mean radius determined from thin section measurements
254 (Fig. 2). The mean quartz radius in the sieve fraction from the PM samples is only slightly smaller
255 than the mean radius from thin section measurements, and the two distributions show significant
256 overlap. Given the good agreement between mean spherical equivalent radii for the sieve fraction
257 and thin section quartz, we assume that the grain size has not been substantially reduced by sample
258 crushing and use the mean and standard deviation of the sieve fraction radii distributions as the
259 appropriate diffusion lengthscale for modeling the diffusion of cosmogenic ^{3}He in each sample.
260
261 **RESULTS**
262 We report measured abundances of cosmogenic ^{3}He in quartz aliquots from each of the Gesso
263 Valley samples in Table 2. We used version 3 (v3) of the online exposure age calculator code, a
264 more recent version of the code published in Balco et al. (2008) that implements the cosmogenic
265 ^{3}He production rate in quartz determined by Vermeesch et al. (2009), to calculate an apparent
266 exposure age from the measured ^{3}He abundance in each aliquot. We assume that the erosion rate
267 is negligible for all boulders sampled, as was assumed in the original publications reporting ^{10}Be
268 exposure ages from these boulders (Federici et al., 2008, 2012). Sample coordinates, elevations,
269 thicknesses, and shielding correction factors used in exposure age calculations are reported in
270 Table 1. In Table 3, we report the weighted mean apparent ^{3}He exposure age for each sample
271 determined using the scaling scheme of Stone (2000). We also recalculated the ^{10}Be exposure ages,
272 normalizing the ^{10}Be concentrations to the isotope ratio standards of Nishiizumi et al. (2007), using

v3 of the online exposure calculator with version 1.1 of the muogenic production rate code and the CRONUS-Earth calibration data set for ^{10}Be production rate (Borchers et al., 2016), and using the scaling scheme of Stone (2000) (Table 3). Our choice to use the global ^{10}Be production rate calibration dataset in Borchers et al. (2016) over a local ^{10}Be production rate calibration (Claude et al., 2014) does not substantially influence the results presented herein. Because the production rates of ^{3}He and ^{10}Be in quartz are not determined from the same calibration datasets, we use the external uncertainties in exposure ages in all calculations that follow. We divided the weighted mean apparent ^{3}He exposure ages by the ^{10}Be exposure ages (both with external uncertainties) to calculate ^{3}He retention, which represents the fraction of cosmogenic ^{3}He produced during surface exposure that remains in the quartz analyzed (Tremblay et al., 2014a).

Fig. 3 shows ^{3}He retention as a function of exposure duration in the five samples we analyzed. All Gesso Valley samples retain less than 50% of the cosmogenic ^{3}He that was produced during their exposure (Table 3, Fig. 3). Retention generally decreases with increasing exposure duration: quartz from PDP10, sampled from the highest elevation moraine with an exposure age of 14071 ± 1220 years, retains 46% of its cosmogenic ^{3}He, while quartz from TDB1, sampled from the lowest elevation moraine with an exposure age of 23397 ± 2072 years, retains only 6% of its cosmogenic ^{3}He. In cases where we have multiple samples from the same moraine, we observe significant intra-moraine differences in ^{3}He retention. PM1 and PM4, both from the Ponte Murato moraine with exposure ages of 16356 ± 1023 and 19213 ± 799 years, respectively, have ^{3}He retentions of 0.28 ± 0.04 versus 0.36 ± 0.04 (Table 3, Fig. 3). Similarly, the two Tetti del Bandito moraine

294 samples TDB1 and TDB3, with exposure ages of 23397 ± 1085 and 21003 ± 965, respectively,
295 have ^{3}He retentions of 0.06 ± 0.01 versus 0.29 ± 0.04 (Table 3, Fig. 3).
296
297 In order to (1) calculate effective diffusion temperatures (EDTs) and infer temperature histories
298 from the observed ^{3}He retention in quartz from each sample, and (2) assess the differences in ^{3}He
299 retention between samples from the same moraine, we need to know the diffusion kinetics of ^{3}He
300 in each sample. Fig. 4 shows the results of step degassing experiments on proton-irradiated quartz
301 from the Gesso Valley samples in Arrhenius plots where the natural log of diffusivity, calculated
302 from the cumulative fraction of gas released during each heating step (Fechtig and Kalbitzer,
303 1966), is plotted as a function of inverse temperature (gray circles).
304
305 All Gesso Valley quartz samples exhibit some degree of nonlinearity in the Arrhenius plots (Fig.
306 4). While we do not have a mechanistic explanation or model for this type of complex diffusion
307 behavior (Tremblay et al., 2014b), multiple diffusion domain (MDD) models (Lovera and Richter,
308 1989; Harrison et al., 1991; Lovera et al., 1991) can reproduce the nonlinearity observed in
309 laboratory degassing experiments and appear to be relevant to ^{3}He diffusive loss over 10^{3}–10^{4} year
310 timescales, as demonstrated for a geologic case study for which the temperatures during surface
311 exposure are reasonably well known (Tremblay et al., 2014b). We constructed MDD models
312 optimized to fit each of the helium step degassing experiments on Gesso Valley quartz samples
313 following the approach outlined in Tremblay et al. (2017). Fig. 5 shows the misfit between the
314 calculated diffusivities from MDD models and the experimentally-determined diffusivities as a

function of number of diffusion domains, where the misfit statistic was calculated as in Tremblay et al. (2017). The misfit shown for a given number of diffusion domains is the minimum misfit found after searching over a large range of model parameters (activation energy E_a, pre-exponential factor(s) D_0/a^2, and gas fraction(s)).

We found that, for all five step degassing experiments, increasing the number of diffusion domains from 1 to 2 and from 2 to 3 significantly reduced the misfit between the observed diffusivities and those calculated with the MDD model (Fig. 5). However, increasing the number of diffusion domains from 3 to 4 did not significantly reduce the misfit between the observed and calculated diffusivities (Fig. 5). For experiment PM1-A, attempts at constructing a four domain model yielded two domains with the same pre-exponential factor and thus are the equivalent of the three domain model. Therefore for all experiments we use the diffusion parameters corresponding to the optimized three domain model. Lines corresponding to the diffusion parameters of the three domains, as well as the calculated diffusivities for the three domain models, are shown in color over the experimentally determined diffusivities in Fig. 4. The activation energies, pre-exponential factors, gas fractions, and misfit statistic for these three domain models are reported in Table 4.

As discussed in Section 2, we need to scale the diffusion kinetics determined from the step degassing experiments to the diffusion lengthscale appropriate for the cosmogenic ^{3}He abundance measurements. In constructing MDD models, we cannot independently parameterize the diffusivity at infinite temperature, D_0, and the diffusion lengthscale, a. Instead, we model them

together as the natural logarithm of the pre-exponential factor in the Arrhenius expression, $ln(D_0/a^2)$, which in an Arrhenius plot corresponds to the y-intercept. Because we cannot independently model the diffusion lengthscale a, we must make an assumption about how to scale the MDD models appropriately. This is not a problem for the $^{40}Ar/^{39}Ar$ thermochronometry community in which MDD models were developed, because in almost all cases argon diffusion kinetics and naturally-occurring argon isotope abundances are measured in the same mineral grain (e.g., Lovera et al., 1997/8). Here, we assume that the diffusion lengthscale of all domains, and by inference all the pre-exponential factors in a given MDD model, scales with the spherical equivalent radius of the quartz grain analyzed. Theoretically, this implies that diffusion lengthscale of the most retentive domain (the domain with the lowest $ln(D_0/a^2)$ or intercept in Arrhenius space) is the spherical equivalent radius of the grain analyzed. Practically, this scaling is accomplished as follows:

$$\left(\frac{D_0}{a^2}\right)_{scaled} = \left(\frac{D_0}{a^2}\right)_{MDD} \left(\frac{a_{sde}^2}{a_{cosmo}^2}\right) \quad \textbf{(1)}$$

where a_{sde} is the spherical equivalent radius of the step degassing experiment quartz grain and a_{cosmo} is the spherical equivalent radius of the quartz grains used for the cosmogenic ^3He measurements (Fig. 2).

With the scaled, sample-specific diffusion kinetics, we explore possible temperature scenarios to

356 explain the observed cosmogenic ^{3}He abundances in the Gesso Valley samples. To do this, we use
357 forward models of simultaneous production and diffusion to model how cosmogenic ^{3}He retention
358 evolves as a function of exposure duration under different temperature scenarios. We begin with
359 the simplest possible scenario of constant temperature over time. Although constant temperatures
360 are not climatologically realistic, this calculation allows us to determine the EDT, which is the
361 temperature corresponding to the mean diffusivity for a given temperature history, that is
362 consistent with the observed cosmogenic ^{3}He retention of each sample. These EDTs are equal to
363 or greater than the true mean temperatures the samples experienced over their exposure durations
364 because of the nonlinear relationship between diffusivity and temperature (Tremblay et al., 2014a).
365 Fig. 6 shows the evolution of ^{3}He retention as a function of exposure duration for constant
366 temperature scenarios in 2 ºC increments from 0 ºC to 30 ºC. These retention evolution curves
367 differ for each Gesso Valley quartz sample for several reasons: (1) each sample has a different set
368 of diffusion kinetics, assuming a three domain diffusion model (Fig. 4, Table 4), (2) these sample
369 specific diffusion kinetics are scaled to different spherical equivalent radii based on the measured
370 grain size distributions of quartz in the sieve fraction used for cosmogenic ^{3}He measurements (Fig.
371 2), and (3) the cosmogenic ^{3}He production rate in quartz differs between samples. In each panel of
372 Fig. 6 we report the integrated EDT that agrees with the observed cosmogenic ^{3}He retention in
373 each quartz sample. We provide two uncertainty estimates on this integrated EDT. One set of EDT
374 uncertainties in parentheses accounts for the uncertainty in ^{3}He retention and exposure duration as
375 determined from ^{10}Be measurements; the second set of uncertainties also accounts for uncertainty
376 in the spherical equivalent radius to which the experimentally-determined diffusion kinetics are

377 scaled.

378

379 The most readily observable feature of the models in Fig. 6 is that the integrated EDT calculated
380 for each quartz sample is different. This is in part expected because the different moraines
381 represented by these samples are located at different elevations in the Gesso Valley, and thus will
382 experience different temperatures at any point in time due to the atmospheric lapse rate. This may
383 also in part be due to the samples having different exposure durations; for example, a change in
384 temperature between the deposition of the TDB moraine and the PM moraine would only be
385 reflected in the cosmogenic ^{3}He retention and integrated EDT of the TDB moraine samples.
386 Differences in integrated EDT between samples from the same moraine, on the other hand, are
387 unexpected. For PM1 we calculate an integrated EDT of 7.6 ºC, while for PM4 we calculate a
388 much higher integrated EDT of 19.7 ºC. Similarly, for TDB1 we calculate an integrated EDT of
389 24.5 ºC, while for TDB3 we calculate a much lower integrated EDT of 15.8 ºC. These intra-
390 moraine discrepancies preclude a straightforward inversion for changes in EDT through time in
391 the Gesso Valley from the inter-moraine differences in ^{3}He retention. We explore possible causes
392 for these intra-moraine discrepancies in the discussion section; here, we compare our observations
393 to modern and paleoclimate observations and simulations to assess whether the EDTs we calculate
394 are plausible for the Gesso Valley since the LGM.

395

396 To contextualize these EDTs integrated over the exposure duration of each sample, in Fig. 7 we
397 use modern daily temperature records from 2002 to 2016 to calculate present-day mean

398 temperatures (solid lines) and EDTs (dashed lines) at the elevation of each moraine. We might
399 expect present-day EDTs at each moraine to be comparable to or greater than the EDT integrated
400 over the samples' exposure durations, considering that mean temperatures during the early, pre-
401 Holocene exposure history of each sample were likely lower than today. However, this expectation
402 may be overly simplistic, as changes in the amplitude of daily and seasonal temperatures since the
403 LGM will also affect the integrated EDTs. Nonetheless, calculation of modern EDTs provides an
404 estimate for the magnitude of the difference between mean temperatures and EDTs due to
405 temperature variations on daily and seasonal timescales in the Gesso Valley.
406
407 We obtained temperature records at the elevation of each moraine by scaling daily mean,
408 minimum, and maximum temperature data from two meteorological stations within the Gesso
409 Valley: Diga della Piastra (44.227 ºE, 7.389 ºN, 959 m) and Diga del Chiotas (44.168 ºE, 7.334
410 ºN, 1980 m). These data are publicly available through the Environmental Protection Agency for
411 the Piemonte Region (arpa.piemonte.gov.it). We scaled the temperature data at Diga della Piastra
412 to the elevation of the TDB and PM moraines and the temperature data at Diga del Chiotas to the
413 elevation of the PDP moraine using monthly average lapse rates determined from the same dataset
414 (minimum = 2.8 ºC/km in December/January; maximum = 6.7 ºC/km in May), and calculated the
415 modern EDT using these scaled temperature data and the activation energies of the best fit MDD
416 models in Fig. 4 and Table 4. The modern EDTs at the three morain elevations are ~4–5 ºC greater
417 than the mean temperatures, reflecting the effect of daily and seasonal temperature amplitudes on
418 the mean diffusivity and EDT. We do not observe a consistent relationship between modern EDT,

419 calculated at the elevation of each moraine, and integrated EDTs calculated for each sample. For
420 PM4 and TDB1, the modern EDT estimate (15.1 and 15.9 ºC) is several degrees lower than the
421 EDT integrated over each sample's exposure duration (19.7 +3.5/–3.7 and 24.5 +4.3/–3.9 ºC). In
422 contrast, the modern EDT estimates for PDP10 and TDB3 (9.8 and 15.9 ºC) are comparable to the
423 EDTs integrated over their exposure durations (13.8 +4.3/–5.7 and 15.8 +3.9/–4.5 ºC), and for
424 PM1 the modern EDT estimate (15.0 ºC) is several degrees higher (vs. 7.6 +3.5/–3.4 ºC).
425
426 In addition to comparing the integrated EDTs calculated from observed cosmogenic ^{3}He
427 abundances to modern day EDTs in the Gesso Valley, we can compare our cosmogenic ^{3}He
428 observations to those that would result from (1) temperature histories simulated in general
429 circulation models (GCMs), and (2) temperature reconstructions based on other proxies at nearby
430 locations. GCM simulations and independent proxy reconstructions provide more realistic late
431 Quaternary temperature scenarios with which to test the plausibility of our cosmogenic ^{3}He
432 observations. As cosmogenic noble gas paleothermometry is refined and improved, cosmogenic
433 ^{3}He observations may also be useful for assessing the fidelity of these paleoclimate simulations
434 and reconstructions based on other proxies. For both model and proxy comparisons, the
435 temperature history used to model cosmogenic ^{3}He abundances must be equal in duration to the
436 moraine sample exposure.
437
438 Most GCM paleo-experiments simulate climate at a particular point in time, such as the mid-
439 Holocene or LGM; only a handful of GCMs simulations have explored transient climate evolution

440 in the Holocene and latest Pleistocene. Here, we model how cosmogenic ^{3}He retention would
441 evolve as a function of exposure duration using seasonal temperature outputs from the TraCE-
442 21ka transient simulation. TraCE-21ka uses the National Center for Atmospheric Research
443 (NCAR) Community Climate System Model version 3 (CCSM3), a synchronously coupled
444 atmosphere-ocean general circulation model (GCM) (Collins et al., 2006), to simulate the Earth's
445 climate from the LGM (22 thousand years ago) to the present (Liu et al., 2009; He, 2011). We
446 obtained mean and maximum seasonal (DJF, MAM, JJA, and SON) temperatures from the TraCE-
447 21ka simulation for the 44.3 ºN, 7.4 ºE grid cell including the Gesso Valley. We chose mean and
448 maximum seasonal temperatures for practical reasons (sub-seasonal temporal resolution is
449 computationally unwieldy), but also because these represent endmember EDT scenarios for the
450 moraines in Gesso Valley. Mean seasonal temperatures represent the low-EDT endmember, as this
451 scenario implies that the mean temperatures represent the full amplitude of seasonal temperature
452 variation and that there is no sub-seasonal (e.g., daily) variability. Maximum seasonal temperatures
453 represent the high-EDT endmember, as this scenario implies that the maximum sub-seasonal
454 temperature simulated during a three month interval is the temperature over the duration of that
455 season. We thus expect the observed cosmogenic ^{3}He retention in our samples to be bracketed by
456 the predicted cosmogenic ^{3}He retention from these endmember scenarios, with the mean seasonal
457 temperature scenario placing an upper bound on cosmogenic ^{3}He retention and the maximum
458 seasonal temperature placing a lower bound.
459
460 TraCE-21ka simulation temperatures were determined for a mean elevation above sea level for the

461 grid cell, which changed through the simulation as simulated sea level changed. However, the
462 elevation of our sample sites with respect to sea level would have also changed through time,
463 meaning that the relative offset between our sample site elevation and the mean grid cell elevation
464 would have remained constant. We therefore scale the TraCE-21ka simulation temperatures to our
465 sample sites using the present day difference between the sample site elevations and TraCE-21ka
466 mean elevation assuming the modern seasonal lapse rate determined from the meteorological
467 stations discussed above. The atmospheric lapse rate in the Gesso Valley likely changed between
468 the LGM and the present, especially considering the fact that the valley was more extensively
469 glaciated during part of this interval. Nonetheless, we assume the modern rate because (1) we have
470 no independent means for assessing how different paleo-lapse rates may have been, and (2) any
471 differences from the modern lapse rate when the valley was glaciated were likely ≤ 2 ºC/km (e.g.,
472 Davis et al., 2003; Gardner et al., 2009; Loomis et al., 2017), which will not be resolvable using
473 our cosmogenic noble gas observations that span ≤ 1 km in elevation (Tremblay et al., 2014a).
474
475 For all Gesso Valley quartz samples, the observed cosmogenic ^{3}He retention is bracketed by the
476 ^{3}He retention calculated assuming mean seasonal temperatures and the ^{3}He retention calculated
477 assuming maximum seasonal temperatures scaled from the TraCE-21ka simulation. For PDP10
478 (Fig. 8), PM4 (Fig. 9), and TDB1 (Fig. 10), we calculate cosmogenic ^{3}He retention from the
479 TraCE-21ka simulation maximum seasonal temperature that is in agreement within uncertainty
480 with the observed retention in these samples. Cosmogenic ^{3}He retention calculated from the
481 TraCE-21ka mean seasonal temperatures agrees with the observed cosmogenic ^{3}He retention in

PM1 within uncertainty (Fig. 9), while for TDB3 the observed cosmogenic ^{3}He retention lies between that predicted from the mean and maximum seasonal TraCE-21ka temperatures.

Lateglacial and Holocene temperatures have been reconstructed from fossil pollen and chironomid records proximal to our study area (e.g. Larocque and Finsinger, 2008; Ortu et al., 2008). Unfortunately, the pollen-based reconstructions of temperature from high-elevation sites in the Maritime Alps are not numerically reported in full (Ortu et al., 2008), preventing us from making a direct comparison with our cosmogenic ^{3}He observations. Thus, here we use chironomid-based July temperature reconstructions from a number of nearby Alpine locations to model cosmogenic ^{3}He retention for comparison with our cosmogenic ^{3}He observations. We spliced together chironomid records from several locations to obtain coeval coverage with samples PDP10 and PM1, which have the youngest ^{10}Be exposure ages of 14071 ± 1220 and 16356 ± 1601 years, respectively. The lack of Alpine chironomid records before 16 cal. years BP prevents us from using chironomid-based July temperature reconstructions to model cosmogenic ^{3}He retention in PM4, TDB1, and TDB3. Like the maximum seasonal temperatures from the TraCE-21ka simulation, we treat the mean July temperature inferred from chironomids as a high-EDT endmember scenario, as this scenario implies that the mean July temperature is representative of sub-annual temperatures.

The most proximal chironomid-based mean July temperature reconstruction is from Lago Piccolo di Avigliana (LPA), located in the Italian Alps ~80 km north of the Gesso Valley (45.05 ºN; 7.38

ºE, 365 m), where the record extends from 14200 to 9500 cal. year BP (Larocque and Finsinger, 2008). In order to obtain coeval coverage with the exposure ages of PDP10 and PM1, we spliced the LPA record with chironomid July temperature reconstructions from: Schwarzsee ob Sölden (SOS), a high-alpine lake in the Austrian Alps (46.96583 ºN, 10.94611 ºE, 2796 m) with a chironomid record from 10200 to –36 cal. years BP (Ilyashuk et al., 2011); Lac Lautrey (LAU), a small lake in the French Jura Mountains (46.58722 ºN, 5.86389 ºE, 788 m) with a chironomid record from 15908 to 11033 cal. years BP (Heiri and Millet, 2005); and Hinterburgsee (HIN), a subalpine lake in the northern Swiss Alps (46.71833 ºN, 8.06750 ºE, 1515 m) with a chironomid record from from 12210 to 1900 cal. years BP (Heiri et al., 2004). Like the GCM simulation, we scaled the July temperature reconstructions from each location to the elevations of PDP10 and PM1 using modern lapse rate information, and when temporal overlap occurred between two or more chironomid records we used an average of the scaled temperatures weighted by the inverse distance between the chironomid sites and our study site.

In Figs. 8 and 9 we show the scaled, spliced July temperature reconstruction using all four chironomid records and the corresponding model for cosmogenic ^{3}He retention in PDP10 and PM1, respectively. We found that different chironomid record splices (e.g., SOS + LPA; SOS + HIN + LPA; SOS + LPA + LAU; SOS + HIN + LPA +LAU) result in very small differences in modeled cosmogenic ^{3}He retention; therefore only the four record splice (SOS + HIN + LPA +LAU) is shown. Like the maximum seasonal temperatures from the TraCE-21ka simulation, we model cosmogenic ^{3}He retention from the mean July temperature reconstruction that agrees with

524 our observations from PDP10 and that underestimates the observed ^{3}He retention in PM1.

525

526 **DISCUSSION**

527 To a first order, the fact that cosmogenic ^{3}He retention calculated with endmember temperature
528 scenarios from a GCM simulation and an independent proxy reconstruction brackets our
529 cosmogenic ^{3}He observations indicates that the ^{3}He observations record ambient temperatures with
530 some accuracy. The observation that our integrated EDTs are not tens of degrees different from
531 modern EDTs in the Gesso Valley calculated with meteorological data also indicates accuracy, as
532 temperature differences between the present-day and LGM were unlikely to exceed 15 ºC (e.g.,
533 Becker et al., 2016), and post-LGM temperature differences were likely to be much smaller. This
534 first order agreement suggests that our cosmogenic ^{3}He measurements are providing meaningful
535 information on ambient temperature conditions during exposure. For example, we do not calculate
536 integrated EDTs below 0 ºC, as we do for cosmogenic ^{3}He measurements made on Holocene-age
537 glacial erratics in Antarctica (Tremblay et al., 2014a), nor do we calculate integrated EDTs
538 unfeasibly high for Earth surface conditions (e.g, EDTs of 70–80 ºC that we obtain for the Moon
539 (Shuster and Cassata, 2015)). However, for the purposes of reconstructing past climate variations,
540 the substantial intra-moraine differences in EDTs are problematic, precluding us from carrying out
541 a straightforward inversion for changes in EDT through time in the Gesso Valley from the inter-
542 moraine differences in ^{3}He retention. For both the PM and TDB moraines, the difference in
543 integrated EDTs between samples from the same moraine is ~10 ºC. These intra-moraine
544 differences require explanation.

One possibility is that these intra-moraine temperature differences are real and reflect differential shading of the samples by vegetation, snow cover or topography. For example, patchy vegetation on a moraine crest may cause one boulder to be fully shaded under a tree canopy, while another boulder tens of meters away remains unshaded. Similarly, boulders nearby to one another might accumulate substantial or insignificant snow cover depending on their relative positioning and shielding from prevailing winds during the wintertime. Unshaded rock samples can experience significantly higher daytime temperatures due to insolation than shaded samples. As discussed in Tremblay et al. (2014a), heating of rocks due to incident solar radiation can substantially raise rock temperatures above daily maximum air temperatures. Amplification of temperatures 5–10 ºC above the daily maximum is common in non-desert environments (McGreevy, 1985; Hall et al., 2005; Bartlett et al., 2006; Schwarz et al., 2012). Considering our modern EDT calculations from meteorological station data, if we increase the maximum daily temperature by 5 or 10 ºC, we find significant increases in the EDT. For example, using the diffusion kinetics for TDB1, by increasing the maximum daily temperature in the meteorological data by 5 ºC, we find that EDT increases from 15.9 to 19.2 ºC. Increasing the maximum daily temperature by 10 ºC increases the EDT to 23.0 ºC, which is within the uncertainty of the EDT integrated over TDB1's exposure duration. Therefore it is possible that, in the case of the TDB moraine, TDB3 may have been shaded or snow covered during part of its exposure history, while TDB1 was fully exposed to incoming solar radiation throughout its exposure. Similarly, PM1 may have been shaded by vegetation or snow covered during periods of time when PM4 was not.

This interpretation is consistent with the comparison of observed cosmogenic ^{3}He retention to calculated retention from TraCE-21ka and chironomid temperatures. Observations from PDP10, PM4, and TDB1 are closest to the TraCE-21ka simulation maximum seasonal temperature calculations, while observations from PM1 are closer to the calculations with the mean seasonal temperature and observations from TDB3 lie between the predicted ^{3}He retention from mean and maximum seasonal temperature scenarios. We would expect mean temperatures to agree with our cosmogenic ^{3}He observations, as is the case for PM1, if no heating due to insolation occurred. Following the same reasoning, we anticipate that samples experiencing nonzero insolation will have cosmogenic ^{3}He abundances that are lower than what is expected from mean air temperatures, as is the case for PDP10, PM4, TDB1, and TDB3. Likewise, the apparent agreement between the observed cosmogenic ^{3}He retention in PDP10 and the chironomid-based reconstruction of mean July temperatures, which will be significantly greater than mean temperatures throughout most of the year, supports the interpretation that the temperatures experienced by sample PDP10 exceeded air temperatures during its exposure to cosmic ray particles. A more precise relationship between insolation-induced daily rock temperature amplifications and maximum seasonal air temperatures or mean July air temperatures could be obtained by monitoring *in situ* rock temperatures adjacent to meteorological stations, such that these temperature scenarios could be adjusted and provide more information than just a high-EDT endmember.

We note that shading from solar radiation and shielding of cosmic rays are not equivalent.

587 Vegetative cover can have a substantial effect on heating by insolation, but in most cases a
588 negligible effect on cosmogenic nuclide production rates due to its relatively low density.
589 Similarly, thin snow cover will not substantially affect cosmogenic nuclide production rates but
590 will cause rock temperatures to differ substantially from air temperatures. Thick snow cover (≥ 1
591 m) will affect both production rates and temperatures. Today, there is significant vegetation cover
592 on the TDB and PM moraines, but no cover at PDP. Unfortunately, we have no way of assessing
593 the degree of vegetation cover on the TDB and PM moraines before the modern era, and no way
594 to assess the past degree of snow cover for all moraines (although observations of in situ 14C in
595 quartz could help address snow cover; e.g., Hippe et al., 2014). Topography can shield rocks from
596 cosmic ray particles, but these effects are accounted for in our calculations of cosmogenic nuclide
597 production rates (Table 1); in contrast, we have not accounted for the effects of topographic
598 shading on rock surface temperatures. We do not have detailed enough locations for the TDB and
599 PM samples to identify the original boulders that were sampled and assess differences in
600 topographic shading, although we suspect this would be secondary to vegetation and snow cover
601 effects.
602
603 Another possible explanation for the intra-moraine differences is that our MDD model
604 representations of helium diffusion kinetics in Gesso Valley quartz samples are inaccurate and/or
605 inadequate. The MDD models we construct are inherently non-unique, and while the models we
606 use minimize the misfit between the observed and calculated diffusivities in our step degassing
607 experiments for a given number of domains, comparable fits can be achieved over a range of

608 diffusion parameters. To illustrate this, in Fig. 11 we show minimized values of MDD model
609 misfit, calculated using the misfit statistic defined in Tremblay et al. (2017), as a function of
610 activation energy E_a for three domain models fit to each of the step degassing experiments shown
611 in Fig. 4. For most of the step degassing experiments, there is a broad range of activation energies
612 (and associated pre-exponential factors and gas release fractions) over which the misfit with the
613 MDD model changes only slightly; these changes in misfit are much smaller than the change in
614 misfit associated with increasing the number of diffusion domains and the model complexity (Fig.
615 5).
616
617 For example, the MDD misfit for the PM1-A step degassing experiment ranges between 7.0 and
618 10.2% between activation energies of 80 and 97.5 *kJ/mol* (Fig. 11). The MDD diffusion kinetics
619 we use in the forward models for PM1 quartz presented above assume an activation energy of 89.6
620 *kJ/mol*. If instead we use a different set of diffusion kinetics for a three domain model that yields
621 a comparable misfit with the step degassing experiment (E_a = 97.5 *kJ/mol*; $ln(D_0/a^2)$ = 12.2, 10.1,
622 16.8; f_{gas} = 0.45, 0.44, 0.11; Misfit = 0.095), we calculate an integrated EDT from the cosmogenic
623 ^{3}He retention in PM1 quartz of 17.8 (± 2.3) +3.8/-3.9 ºC, which is in agreement with the integrated
624 EDT we calculated for PM4 (Fig. 6). This highlights how sensitive the temperatures we calculate
625 from an observed amount of cosmogenic ^{3}He retention are to the diffusion kinetics we use. While
626 different MDD models might reproduce diffusivities observed in laboratory step degassing
627 experiments comparably well, the downward extrapolation of these models results in significantly
628 different diffusivities at the temperatures characterizing Earth's surface. This suggests that some

or all of the intra-moraine differences in integrated EDTs could be attributed to uncertainties in how we extrapolate laboratory-determined diffusion kinetics. Given that we do not yet have a mechanistic understanding of what controls the complex noble gas diffusion behavior we observe in our experiments, discriminating between different MDD models of comparably good fit (and even assessing whether MDD models adequately represent the processes responsible for complex behavior) is difficult at this stage.

A third possible explanation for the intra-moraine variation could arise from our grain size analysis and scaling of MDD models. Uncertainty in the physical significance of our MDD models translates into an uncertainty in our assumptions about how to scale our MDD model fits from step degassing experiments to the cosmogenic ^{3}He measurements. However, because we have scaled the results of each experiment using the same assumptions in Eq. 1, the effects will be systematic. Similarly, the factor of 1.5 we applied to estimated spherical equivalent radii of quartz from the sieve fractions, based on different approaches to estimate surface area to volume ratios and ground truthing with x-ray computed tomography data, will have systematic effects on all integrated EDTs. Assuming that the MDD model scaling and correction applied to sieve fraction measurements are appropriate, we must also consider the possibility that our grain size analysis for the PM and TDB samples does not represent the actual grain size and diffusion lengthscale of quartz in these samples. Since we did not have whole rock material from the original PM and TDB samples, we made thin sections from other boulders collected from the PM and TDB moraines to compare with the size distributions of quartz in the sieved fraction. While there is good agreement

between the mean spherical equivalent radii of quartz measured in these thin sections and in the sieve fractions, it is possible that in the original sample the mean quartz size before crushing was much larger. As a sensitivity test, we again use PM1 as an example. In order to obtain an integrated EDT for PM1 equivalent to that calculated for PM4 of 19.7 ºC, we must increase the spherical equivalent radius assumed for the cosmogenic ^{3}He measurement by 110% (without changing the spherical equivalent radius for PM4). While such a dramatic underestimation of the PM1 grain size, and more generally >100% uncertainty in all our PM and TDB grain size analyses, seems unlikely, we cannot rule out such a possibility given that whole rock material from these samples was unavailable.

As a final potential source of intra-moraine variation, the moraine boulders that we sampled may have more complex exposure histories than we allow for in our production and diffusion models, either due to cosmogenic ^{10}Be and ^{3}He inheritance or due to nonzero erosion rates that vary between boulders. More complex exposure histories are plausible for all three moraines, as the ^{10}Be exposure ages from a given moraine do not overlap within their internal uncertainties (Table 3). Although we only studied one boulder from the PDP moraine, cosmogenic ^{10}Be measurements for four additional PDP boulders also exhibit dispersion that cannot be explained by measurement uncertainty alone (Federici et al., 2008). PDP10, the sample studied here, has the oldest exposure age of the five boulders with ^{10}Be measurements. We do not have measurements of additional cosmogenic nuclides (e.g., *in situ* ^{14}C) to test whether our samples exhibit evidence for complex exposure. Nonetheless, we can explore what effects inheritance and nonzero erosion might have

671 on our cosmogenic ^{3}He observations and the EDTs we calculate from them.

672

673 Inheritance would most likely affect the boulders from each moraine with the oldest apparent ^{10}Be
674 exposure ages: PDP10, PM4, and TDB1. The cosmogenic ^{3}He observations from these boulders
675 yield higher integrated EDTs than other boulders from the same moraine (in the case of PM4 and
676 TDB1) and are closest to the ^{3}He retention calculated using the high-EDT endmember scenarios
677 (maximum seasonal temperatures from TraCE-21ka and mean July temperatures from spliced
678 chironomid records). In order for inheritance to explain these observations and the intra-moraine
679 differences in integrated EDT, the quartz in these boulders would have to lose a substantial
680 proportion of their inherited ^{3}He relative to inherited ^{10}Be. This is not unreasonable considering
681 that temperature-dependent diffusive loss would also affect cosmogenic ^{3}He produced prior to
682 boulders being deposited in a moraine; thus we consider inheritance to be a viable option to explain
683 some of the intra-moraine discrepancies we observe.

684

685 In contrast, nonzero erosion rates will likely affect the boulders from each moraine with the
686 youngest apparent ^{10}Be exposure ages: PM1 and TDB3. The cosmogenic ^{3}He observations from
687 these boulders yield lower integrated EDTs than other boulders from the same moraine and are
688 closer to the ^{3}He retention calculated using the low-EDT endmember scenario (mean seasonal
689 temperatures from TraCE-21ka). If we assume that 15 cm of material has been eroded since the
690 initial exposures of PM1 and TDB3–corresponding to the depth at which daily temperature
691 oscillations typically become negligible in rock (Tremblay et al., 2014a)–and that the exposure

692 ages calculated from ^{10}Be measurements from PM4 and TDB1 are the respective true exposure
693 ages, we can recalculate the ^{10}Be exposure age, ^{3}He apparent exposure age, and ^{3}He retention for
694 PM1 and TDB3. This results in an increase in ^{10}Be exposure age (e.g., from 16356 ± 1023 to 18821
695 ± 1335 for PM1), but not a substantial decrease in ^{3}He retention (e.g., from 0.28 ± 0.04 to 0.25 ±
696 0.04 for PM1). As a consequence, the integrated EDTs we would calculate for these samples
697 including the effects of erosion would not be substantially higher than those we calculated
698 assuming no erosion. A similar effect is expected if, rather than erosion of the boulder surfaces
699 themselves, the boulders were initially shielded by a variable thickness of sediment cover that has
700 since eroded (e.g., Putkonen and Swanson, 2003; Heyman et al., 2011). Thus the effects of variable
701 erosion seem unlikely to fully explain the intra-moraine differences we observe.
702
703 In summary, there is substantial intra-moraine variability in the integrated EDTs we calculate from
704 our cosmogenic ^{3}He observations that requires explanation. We have outlined four major sources
705 of uncertainty in our approach that could explain these intra-moraine variations. Ultimately, these
706 potential sources of uncertainty are too under-constrained at this time to allow for a straightforward
707 interpretation about the climate history of the Maritime Alps during deglaciation from our
708 cosmogenic noble gas data. Nonetheless, we calculate integrated EDTs for all samples that are
709 bracketed by plausible endmember EDT scenarios for the Gesso Valley based on mean and
710 maximum seasonal temperatures from the TraCE-21ka simulation and on chironomid-derived
711 mean July temperature reconstructions. The trend toward the high-EDT endmember scenarios for
712 all samples except PM1 is not surprising, given that we expect integrated EDTs to exceed the mean

ambient temperatures in a sample's exposure history because of the nonlinear dependence of diffusivity on temperature. The observation that our integrated EDTs are not drastically different from modern EDTs in the Gesso Valley is also encouraging, given the magnitude of plausible temperature differences between the LGM and today. Collectively, these results demonstrate promise for the application of cosmogenic noble gas paleothermometry in paleoclimate studies, provided that the four major sources of uncertainty we detail above are accounted for in future applications.

CONCLUSIONS

Integrated EDTs since the LGM in the Gesso Valley, calculated from our observations of cosmogenic ^{3}He concentrations in quartz, range from 8 to 25 ºC and are consistent with what we expect from modern meteorological station data, a GCM simulation of Earth's climate since the LGM, and data from independent proxies in the region. Nonetheless, there are nontrivial differences between the integrated EDTs we calculate, particularly for samples from the same moraine, that require explanation. We identify four major potential sources of uncertainty that could account for these discrepancies: (1) the fact that we have not accounted for variations in radiative heating of the boulder surfaces across samples due to differential shading, (2) limitations in our understanding of and ability to model and extrapolate helium diffusion kinetics when complex behavior is observed, (3) uncertainties associated with our quartz grain size analyses, and (4) unaccounted for erosion or cosmogenic inheritance. At this stage, all four of these possibilities could be contributing to intra-moraine and inter-moraine variability in reconstructed temperatures.

734 Because of these uncertainties, and the fact that we have no cosmogenic ^{3}He observations from
735 younger moraines that record only Holocene temperatures in the Gesso Valley, it is difficult to
736 fully compare our results to the TraCE-21ka and chironomid temperature records, or to invert our
737 results directly for changes in EDT through time in the Gesso Valley from the inter-moraine
738 differences in ^{3}He retention. As a consequence, it is not yet possible to use these data to test the
739 hypothesis that the post-LGM climate evolution and glacier dynamics of the Maritime Alps
740 differed from other Alpine regions with our dataset. These results nonetheless demonstrate first
741 order accuracy in the temperatures recorded by cosmogenic noble gas paleothermometry, and
742 highlight major sources of uncertainty that can be addressed in future applications to improve how
743 cosmogenic noble gas paleothermometry contributes to paleoclimate studies.
744
745 **ACKNOWLEDGEMENTS**
746 MMT and DLS acknowledge support from the NSF Petrology and Geochemistry Program (EAR-
747 1322086 to DLS), the UC Berkeley Larsen Grant, and the Ann and Gordon Getty Foundation.
748 MMT was supported by an NSF Graduate Research Fellowship. MS acknowledges support from
749 the Royal Society (IE150603), the Leverhulme Trust (IAF-2016-001) and NERC (CIAF
750 9092.1010). AR acknowledges support from the University of Pisa fund PRA (2017). M. Uebner
751 and S. Woodmansee are thanked for help with sample preparation. We also thank Associate Editor
752 Kathleen R. Johnson, Jakob Heyman, and an anonymous reviewer for constructive feedback on
753 this work.
754

REFERENCES CITED

Annan, J.D., Hargreaves, J.C., 2013. A new global reconstruction of temperature changes at the Last Glacial Maximum. Climate of the Past 9, 367–376.

Annan, J.D., Hargreaves, J.C., 2015. A perspective on model-data surface temperature comparison at the Last Glacial Maximum. Quaternary Science Reviews 107, 1–10.

Balco, G., Stone, J.O., Lifton, N.A., Dunai, T.J., 2008. A complete and easily accessible means of calculating surface exposure ages or erosion rates from ^{10}Be and ^{26}Al measurements. Quaternary Geochronology 3, 174–195.

Bartlein, P.J., Harrison, S.P., Brewer, S., Connor, S., Davis, B., Gajewski, K., Guiot, J., Harrison-Prentice, T.I., Henderson, A., Peyron, O., Others, 2011. Pollen-based continental climate reconstructions at 6 and 21 ka: a global synthesis. Climate Dynamics Springer 37, 775–802.

Bartlett, M.G., Chapman, D.S., Harris, R.N., 2006. A decade of ground–air temperature tracking at Emigrant Pass Observatory, Utah. Journal of Climate 19, 3722–3731.

Becker, P., Seguinot, J., Jouvet, G., Funk, M., 2016. Last Glacial Maximum precipitation pattern in the Alps inferred from glacier modelling. Geographica Helvetica 71, 173–187.

Blaga, C.I., Reichart, G.-J., Lotter, A.F., Anselmetti, F.S., Sinninghe Damsté, J.S., 2013. A TEX 86 lake record suggests simultaneous shifts in temperature in Central Europe and Greenland during the last deglaciation. Geophysical research letters 40, 948–953.

Borchers, B., Marrero, S., Balco, G., Caffee, M., Goehring, B., Lifton, N., Nishiizumi, K., Phillips, F., Schaefer, J., Stone, J., 2016. Geological calibration of spallation production

776 rates in the CRONUS-Earth project. Quaternary Geochronology 31, 188–198.
777 Brisset, E., Guiter, F., Miramont, C., Revel, M., Anthony, E.J., Delhon, C., Arnaud, F., Malet, E.,
778 de Beaulieu, J.-L., 2015. Lateglacial/Holocene environmental changes in the
779 Mediterranean Alps inferred from lacustrine sediments. Quaternary Science Reviews
780 110, 49–71.
781 Buckenham, M.H., Rogers, J., 1954. Flotation of quartz and feldspar by dodecylamine.
782 Transactions of Institute of Mining and Metallurgy 64, l–30.
783 Casazza, G., Grassi, F., Zecca, G., Minuto, L., 2016. Phylogeographic Insights into a Peripheral
784 Refugium: The Importance of Cumulative Effect of Glaciation on the Genetic Structure
785 of Two Endemic Plants. PloS one Public Library of Science 11, e0166983.
786 Claude, A., Ivy-Ochs, S., Kober, F., Antognini, M., Salcher, B., Kubik, P.W., 2014. The
787 Chironico landslide (Valle Leventina, southern Swiss Alps): age and evolution. Swiss
788 Journal of Geosciences 107, 273–291.
789 Collins, W.D., Bitz, C.M., Blackmon, M.L., Bonan, G.B., Bretherton, C.S., Carton, J.A., Chang,
790 P., Doney, S.C., Hack, J.J., Henderson, T.B., Others, 2006. The community climate
791 system model version 3 (CCSM3). Journal of Climate 19, 2122–2143.
792 Davis, B.A.S., Brewer, S., Stevenson, A.C., Guiot, J., 2003. The temperature of Europe during
793 the Holocene reconstructed from pollen data. Quaternary Science Reviews 22, 1701–
794 1716.
795 Durand, Y., Giraud, G., Laternser, M., Etchevers, P., Mérindol, L., Lesaffre, B., 2009a.
796 Reanalysis of 47 years of climate in the French Alps (1958–2005): climatology and

trends for snow cover. Journal of Applied Meteorology and Climatology 48, 2487–2512.

Durand, Y., Laternser, M., Giraud, G., Etchevers, P., Lesaffre, B., Mérindol, L., 2009b. Reanalysis of 44 yr of climate in the French Alps (1958–2002): methodology, model validation, climatology, and trends for air temperature and precipitation. Journal of Applied Meteorology and Climatology 48, 429–449.

Fechtig, H., Kalbitzer, S., 1966. The diffusion of argon in potassium-bearing solids. Potassium argon dating. Springer, pp. 68–107.

Federici, P.R., Granger, D.E., Pappalardo, M., Ribolini, A., Spagnolo, M., Cyr, A.J., 2008. Exposure age dating and Equilibrium Line Altitude reconstruction of an Egesen moraine in the Maritime Alps, Italy. Boreas 37, 245–253.

Federici, P.R., Granger, D.E., Ribolini, A., Spagnolo, M., Pappalardo, M., Cyr, A.J., 2012. Last Glacial Maximum and the Gschnitz stadial in the Maritime Alps according to ^{10}Be cosmogenic dating. Boreas 41, 277–291.

Federici, P.R., Pappalardo, M., Ribolini, A., 2003. Geomorphological map of the Maritime Alps Natural Park and surroundings (Argentera Massif, Italy). 1: 25,000 scale. Selca, Florence.

Federici, P.R., Ribolini, A., Spagnolo, M., 2017. Glacial history of the Maritime Alps from the Last Glacial Maximum to the Little Ice Age. Geological Society, London, Special Publications 433, 137–159.

Gandouin, E., Franquet, E., 2002. Late Glacial and Holocene chironomid assemblages in Lac Long Inférieur (southern France, 2090 m): palaeoenvironmental and palaeoclimatic implications. Journal of Paleolimnology 28, 317–328.

818 Gardner, A.S., Sharp, M.J., Koerner, R.M., Labine, C., Boon, S., Marshall, S.J., Burgess, D.O.,
819 Lewis, D., 2009. Near-surface temperature lapse rates over Arctic glaciers and their
820 implications for temperature downscaling. Journal of Climate 22, 4281–4298.
821 Gourbet, L., Shuster, D.L., Balco, G., Cassata, W.S., Renne, P.R., Rood, D., 2012. Neon
822 diffusion kinetics in olivine, pyroxene and feldspar: retentivity of cosmogenic and
823 nucleogenic neon. Geochimica et Cosmochimica Acta 86, 21–36.
824 Granger, D.E., Lifton, N.A., Willenbring, J.K., 2013. A cosmic trip: 25 years of cosmogenic
825 nuclides in geology. Geological Society of America Bulletin 125, 1379–1402.
826 Hall, K., Lindgren, B.S., Jackson, P., 2005. Rock albedo and monitoring of thermal conditions in
827 respect of weathering: some expected and some unexpected results. Earth Surface
828 Processes and Landforms 30, 801–812.
829 Harrison, S.P., Bartlein, P.J., Izumi, K., Li, G., Annan, J., Hargreaves, J., Braconnot, P.,
830 Kageyama, M., 2015. Evaluation of CMIP5 palaeo-simulations to improve climate
831 projections. Nature Climate Change 5, 735–743.
832 Harrison, T.M., Lovera, O.M., Matthew, T.H., 1991. $^{40}Ar/^{39}Ar$ results for alkali feldspars
833 containing diffusion domains with differing activation energy. Geochimica et
834 Cosmochimica Acta 55, 1435–1448.
835 He, F., 2011. Simulating transient climate evolution of the last deglaciation with CCSM 3. PhD,
836 University of Wisconsin-Madison.
837 Heilbronner, R., Barrett, S., 2013. Image analysis in Earth sciences: microstructures and textures
838 of earth materials. Springer.

839 Heiri, O., Brooks, S.J., Renssen, H., Bedford, A., Hazekamp, M., Ilyashuk, B., Jeffers, E.S.,
840 Lang, B., Kirilova, E., Kuiper, S., Others, 2014. Validation of climate model-inferred
841 regional temperature change for late-glacial Europe. Nature Communications 5, 4914.
842 Heiri, O., Millet, L., 2005. Reconstruction of Late Glacial summer temperatures from
843 chironomid assemblages in Lac Lautrey (Jura, France). Journal of Quaternary Science 20,
844 33–44.
845 Heiri, O., Tinner, W., Lotter, A.F., 2004. Evidence for cooler European summers during periods
846 of changing meltwater flux to the North Atlantic. Proceedings of the National Academy
847 of Sciences 101, 15285–15288.
848 Heyman, J., Stroeven, A.P., Harbor, J.M., Caffee, M.W., 2011. Too young or too old: Evaluating
849 cosmogenic exposure dating based on an analysis of compiled boulder exposure ages.
850 Earth and Planetary Science Letters 302, 71–80.
851 Hippe, K., Ivy-Ochs, S., Kober, F., Zasadni, J., Wieler, R., Wacker, L., Kubik, P.W., Schlüchter,
852 C., 2014. Chronology of Lateglacial ice flow reorganization and deglaciation in the
853 Gotthard Pass area, Central Swiss Alps, based on cosmogenic ^{10}Be and in situ ^{14}C.
854 Quaternary geochronology 19, 14–26.
855 Ilyashuk, E.A., Koinig, K.A., Heiri, O., Ilyashuk, B.P., Psenner, R., 2011. Holocene temperature
856 variations at a high-altitude site in the Eastern Alps: a chironomid record from
857 Schwarzsee ob Sölden, Austria. Quaternary Science Reviews 30, 176–191.
858 Ivy-Ochs, S., Kober, F., Alfimov, V., Kubik, P.W., Synal, H.-A., 2007. Cosmogenic ^{10}Be, ^{21}Ne
859 and ^{36}Cl in sanidine and quartz from Chilean ignimbrites. Nuclear Instruments &

Methods in Physics Research B 259, 588–594.

Jost, A., Lunt, D., Kageyama, M., Abe-Ouchi, A., Peyron, O., Valdes, P.J., Ramstein, G., 2005. High-resolution simulations of the last glacial maximum climate over Europe: a solution to discrepancies with continental palaeoclimatic reconstructions?. Climate Dynamics Springer 24, 577–590.

Kessler, M.A., Anderson, R.S., Stock, G.M., 2006. Modeling topographic and climatic control of east-west asymmetry in Sierra Nevada glacier length during the Last Glacial Maximum. Journal of Geophysical Research: Earth Surface 111.

Ketcham, R.A., 2005. Computational methods for quantitative analysis of three-dimensional features in geological specimens. Geosphere 1, 32–41.

Kuhlemann, J., Rohling, E.J., Krumrei, I., Kubik, P., Ivy-Ochs, S., Kucera, M., 2008. Regional synthesis of Mediterranean atmospheric circulation during the Last Glacial Maximum. Science 321, 1338–1340.

Lal, D., 1987. Production of 3He in terrestrial rocks. Chemical Geology 66, 89–98.

Larocque, I., Finsinger, W., 2008. Late-glacial chironomid-based temperature reconstructions for Lago Piccolo di Avigliana in the southwestern Alps (Italy). Palaeogeography, Palaeoclimatology, Palaeoecology 257, 207–223.

Liu, Z., Otto-Bliesner, B.L., He, F., Brady, E.C., Tomas, R., Clark, P.U., Carlson, A.E., Lynch-Stieglitz, J., Curry, W., Brook, E., Others, 2009. Transient simulation of last deglaciation with a new mechanism for Bølling-Allerød warming. Science 325, 310–314.

Loomis, S.E., Russell, J.M., Verschuren, D., Morrill, C., De Cort, G., Damsté, J.S.S., Olago, D.,

881 Eggermont, H., Street-Perrott, F.A., Kelly, M.A., 2017. The tropical lapse rate steepened
882 during the Last Glacial Maximum. Science Advances 3, e1600815.
883 Lovera, O.M., Grove, M., Mark Harrison, T., Mahon, K.I., 1997/8. Systematic analysis of K-
884 feldspar $^{40}Ar/^{39}Ar$ step heating results: I. Significance of activation energy
885 determinations. Geochimica et Cosmochimica Acta 61, 3171–3192.
886 Lovera, O.M., Richter, F.M., 1989. The $^{40}Ar/^{39}Ar$ Thermochronometry for Slowly Cooled
887 Samples. Journal of Geophysical Research 94, 17–917.
888 Lovera, O.M., Richter, F.M., Harrison, T.M., 1991. Diffusion domains determined by ^{39}Ar
889 released during step heating. Journal of Geophysical Research 96, 2057–2069.
890 Luetscher, M., Boch, R., Sodemann, H., Spötl, C., Cheng, H., Edwards, R.L., Frisia, S., Hof, F.,
891 Müller, W., 2015. North Atlantic storm track changes during the Last Glacial Maximum
892 recorded by Alpine speleothems. Nature Communications 6, 6344.
893 Mauri, A., Davis, B.A.S., Collins, P.M., Kaplan, J.O., 2015. The climate of Europe during the
894 Holocene: a gridded pollen-based reconstruction and its multi-proxy evaluation.
895 Quaternary Science Reviews 112, 109–127.
896 Masson-Delmotte, V., Schulz, M., Abe-Ouchi, A., Beer, J., Ganopolski, A., González Rouco,
897 J.F., Jansen, E., Lambeck, K., Luterbacher, J., Naish, T., Osborn, T., Otto-Bliesner, B.,
898 Quinn, T., Ramesh, R., Rojas, M., Shao, X., Timmermann, A., 2013. Information from
899 paleoclimate archives. In: Stocker, T.F., Qin, D., Plattner, G.-K., Tignor, M., Allen, S.K.,
900 Boschung, J., Nauels, A., Xia, Y., Bex, V., Midgley, P.M. (Eds.), Climate Change 2013:
901 The Physical Science Basis. Contribution of Working Group I to the Fifth Assessment

902 Report of the Intergovernmental Panel on Climate Change. Cambridge University Press,
903 pp. 383–464.
904 McGreevy, J.P., 1985. Thermal properties as controls on rock surface temperature maxima, and
905 possible implications for rock weathering. Earth Surface Processes and Landforms 10,
906 125–136.
907 Monegato, G., Scardia, G., Hajdas, I., Rizzini, F., Piccin, A., 2017. The Alpine LGM in the
908 boreal ice-sheets game. Scientific Reports 7, 2078.
909 Nishiizumi, K., Imamura, M., Caffee, M.W., Southon, J.R., Finkel, R.C., McAninch, J., 2007.
910 Absolute calibration of ^{10}Be AMS standards. Nuclear Instruments & Methods in Physics
911 Research B 258, 403–413.
912 Ortu, E., Brewer, S., Peyron, O., 2006. Pollen-inferred Paleoclimate reconstructions in mountain
913 areas: problems and perspectives. Journal of Quaternary Science 21, 615–627.
914 Ortu, E., Peyron, O., Bordon, A., de Beaulieu, J.L., Siniscalco, C., Caramiello, R., 2008.
915 Lateglacial and Holocene climate oscillations in the South-western Alps: An attempt at
916 quantitative reconstruction. Quaternary International 190, 71–88.
917 Putkonen, J., Swanson, T., 2003. Accuracy of cosmogenic ages for moraines. Quaternary
918 Research 59, 255–261.
919 Schmidt, G.A., Annan, J.D., Bartlein, P.J., Cook, B.I., Guilyardi, E., Hargreaves, J.C., Harrison,
920 S.P., Kageyama, M., LeGrande, A.N., Konecky, B., Lovejoy, S., Mann, M.E., Masson-
921 Delmotte, V., Risi, C., Thompson, D., Timmermann, A., Tremblay, L.-B., Yiou, P., 2014.
922 Using palaeo-climate comparisons to constrain future projections in CMIP5. Climate of

923 the Past 10, 221–250.
924 Schmittner, A., Urban, N.M., Shakun, J.D., Mahowald, N.M., Clark, P.U., Bartlein, P.J., Mix,
925 A.C., Rosell-Melé, A., 2011. Climate sensitivity estimated from temperature
926 reconstructions of the Last Glacial Maximum. Science 334, 1385–1388.
927 Schneider, C.A., Rasband, W.S., Eliceiri, K.W., 2012. NIH Image to ImageJ: 25 years of image
928 analysis. Nature Methods 9, 671–675.
929 Schwarz, N., Schlink, U., Franck, U., Großmann, K., 2012. Relationship of land surface and air
930 temperatures and its implications for quantifying urban heat island indicators--An
931 application for the city of Leipzig (Germany). Ecological indicators 18, 693–704.
932 Shuster, D.L., Cassata, W.S., 2015. Paleotemperatures at the lunar surfaces from open system
933 behavior of cosmogenic ^{38}Ar and radiogenic ^{40}Ar. Geochimica et Cosmochimica Acta
934 155, 154–171.
935 Shuster, D.L., Farley, K.A., 2005. Diffusion kinetics of proton-induced ^{21}Ne, ^{3}He, and ^{4}He in
936 quartz. Geochimica et Cosmochimica Acta 69, 2349–2359.
937 Shuster, D.L., Farley, K.A., Sisterson, J.M., Burnett, D.S., 2004. Quantifying the diffusion
938 kinetics and spatial distributions of radiogenic ^{4}He in minerals containing proton-induced
939 ^{3}He. Earth and Planetary Science Letters 217, 19–32.
940 Stone, J.O., 2000. Air pressure and cosmogenic isotope production. Journal of Geophysical
941 Research: Solid Earth 105, 23753–23759.
942 Tremblay, M.M., Shuster, D.L., Balco, G., 2014a. Cosmogenic noble gas paleothermometry.
943 Earth and Planetary Science Letters 400, 195–205.

Tremblay, M.M., Shuster, D.L., Balco, G., 2014b. Diffusion kinetics of ^{3}He and ^{21}Ne in quartz and implications for cosmogenic noble gas paleothermometry. Geochimica et Cosmochimica Acta 142, 186–204.

Tremblay, M.M., Shuster, D.L., Balco, G., Cassata, W.S., 2017. Neon diffusion kinetics and implications for cosmogenic neon paleothermometry in feldspars. Geochimica et Cosmochimica Acta 205, 14–30.

Vermeesch, P., Baur, H., Heber, V.S., Kober, F., Oberholzer, P., Schaefer, J.M., Schlüchter, C., Strasky, S., Wieler, R., 2009. Cosmogenic ^{3}He and ^{21}Ne measured in quartz targets after one year of exposure in the Swiss Alps. Earth and Planetary Science Letters 284, 417–425.

von der Heydt, A.S., Dijkstra, H.A., van de Wal, R.S.W., Caballero, R., Crucifix, M., Foster, G.L., Huber, M., Köhler, P., Rohling, E., Valdes, P.J., Ashwin, P., Bathiany, S., Berends, T., van Bree, L.G.J., Ditlevsen, P., Ghil, M., Haywood, A.M., Katzav, J., Lohmann, G., Lohmann, J., Lucarini, V., Marzocchi, A., Pälike, H., Baroni, I.R., Simon, D., Sluijs, A., Stap, L.B., Tantet, A., Viebahn, J., Ziegler, M., 2016. Lessons on Climate Sensitivity From Past Climate Changes. Current Climate Change Reports 2, 148–158.

LIST OF TABLES

Table 1: Locations and sample information for moraine boulders in the Gesso Valley previously exposure dated with cosmogenic ^{10}Be, originally reported in Federici et al. (2012, 2008).

Sample	Latitude (decimal degrees)	Longitude (decimal degrees)	Elevation (m)	Sample thickness (cm)	Shielding factor
PDP10	44.421534	7.819950	1806	3	0.9200
PM1	44.252667	7.385500	860	3	0.9653
PM4	44.252667	7.385500	860	3	0.9653
TDB1	44.289712	7.432528	770	3	0.9825
TDB3	44.289712	7.432528	770	3	0.9819

964

965 **Table 2:** Observations of cosmogenic ^{3}He in Gesso Valley quartz samples.

Sample - aliquot	Mass of quartz analyzed (g)	[^{3}He] (10^{6} atoms/g)		
PDP10-1	0.109	2.20	±	0.38
PDP10-2	0.101	2.38	±	0.37
PDP10-3	0.102	3.65	±	0.35
PDP10-4	0.126	2.91	±	0.26
PDP10-5	0.121	2.99	±	0.39
PDP10-6	0.136	2.99	±	0.31
PDP10-7	0.117	3.12	±	0.37
PDP10-8	0.125	2.44	±	0.35
PM1-1	0.101	1.14	±	0.42
PM1-2	0.101	0.89	±	0.6
PM1-3	0.304	1.11	±	0.18
PM1-4	0.266	0.88	±	0.15
PM1-5	0.290	1.05	±	0.15
PM4-1	0.113	1.29	±	0.34
PM4-2	0.309	1.51	±	0.17
PM4-3	0.268	1.63	±	0.19
PM4-4	0.247	1.60	±	0.12
TDB1-1	0.216	0.62	±	0.28
TDB1-2	0.269	0.11	±	0.14

TDB1-3	0.306	0.28	±	0.13
TDB1-4	0.292	0.26	±	0.13
TDB1-5	0.482	0.36	±	0.08
TDB3-1	0.216	1.38	±	0.27
TDB3-2	0.124	1.35	±	0.39
TDB3-3	0.279	1.20	±	0.19
TDB3-4	0.301	1.31	±	0.27
TDB3-5	0.268	1.32	±	0.18

966

967

968 **Table 3:** Apparent ^{3}He exposure ages and retention in Gesso Valley quartz samples. See text for
969 details about the input parameters to the exposure age calculation. Because we have measurements
970 of cosmogenic ^{3}He from multiple aliquots of each sample, we report weighted mean apparent
971 exposure ages with internal uncertainties alongside weighted mean apparent exposure ages with
972 external uncertainties in parentheses. Because we only have one ^{10}Be measurement per sample,
973 we report a single ^{10}Be exposure age for each sample with internal uncertainty alongside external
974 uncertainty in parentheses. Cosmogenic ^{3}He retention is calculated using external uncertainties.

Sample	**Weighted mean apparent exposure age (yr), ^{3}He**	**Exposure age (yr), ^{10}Be**	**^{3}He retention**		
PDP10	6513 ± 273 (6402 ± 341)	14071 ± 606(1220)	0.46	±	0.05
PM1	4539 ± 400 (4534 ± 452)	16356 ± 1023(1601)	0.28	±	0.04
PM4	7071 ± 377 (7006 ± 512)	19213 ± 799(1654)	0.36	±	0.04
TDB1	1424 ± 261 (1407 ± 271)	23397 ± 1085(2072)	0.06	±	0.01
TDB3	6178 ± 496 (6187 ± 561)	21003 ± 965(1854)	0.29	±	0.04

975

976 **Table 4:** Three domain multiple diffusion domain model parameters for ^{3}He diffusion experiments
977 in Gesso Valley quartz samples.

Experiment	Domain	E_a (kJ/mol)	$\ln(D_0/a^2)$	fraction	Misfit
PDP10-B	1	96.5	10.2	0.61	0.097
	2		16.1	0.21	
	3		13.2	0.18	
PM1-A	1	89.6	8.6	0.54	0.067
	2		10.1	0.36	
	3		14.1	0.1	
PM4-A	1	90.9	8.4	0.74	0.109
	2		5.9	0.2	
	3		14.4	0.06	
TDB1-B	1	99.7	11.8	0.46	0.161
	2		13.2	0.3	
	3		17.3	0.24	
TDB3-B	1	97.6	10.3	0.42	0.149
	2		12.3	0.41	
	3		15.7	0.17	

978

979 **LIST OF FIGURES**

980 **Figure 1:** A: Topographic map of the Maritime Alps. Map location is shown in the inset of Italy.
981 White box corresponds to the enlarged view in (B). B: Topography of the Gesso Valley. White
982 stars mark the locations of moraines sampled for this study: Piano del Praiet (PDP), Ponte Murato
983 (PM), and Tetti del Bandito (TDB). Dashed line corresponds to the longitudinal profile shown in
984 (C). C: Longitudinal profile of the Gesso Valley. White stars mark the locations of moraines

studied here, as in (B); white circles denote additional moraines in the Gesso Valley not studied here. A detailed map of the geomorphic features in the Gesso Valley is available in Federici et al. (2003). For interpretation of references to color in this figure, refer to the web version of this article.

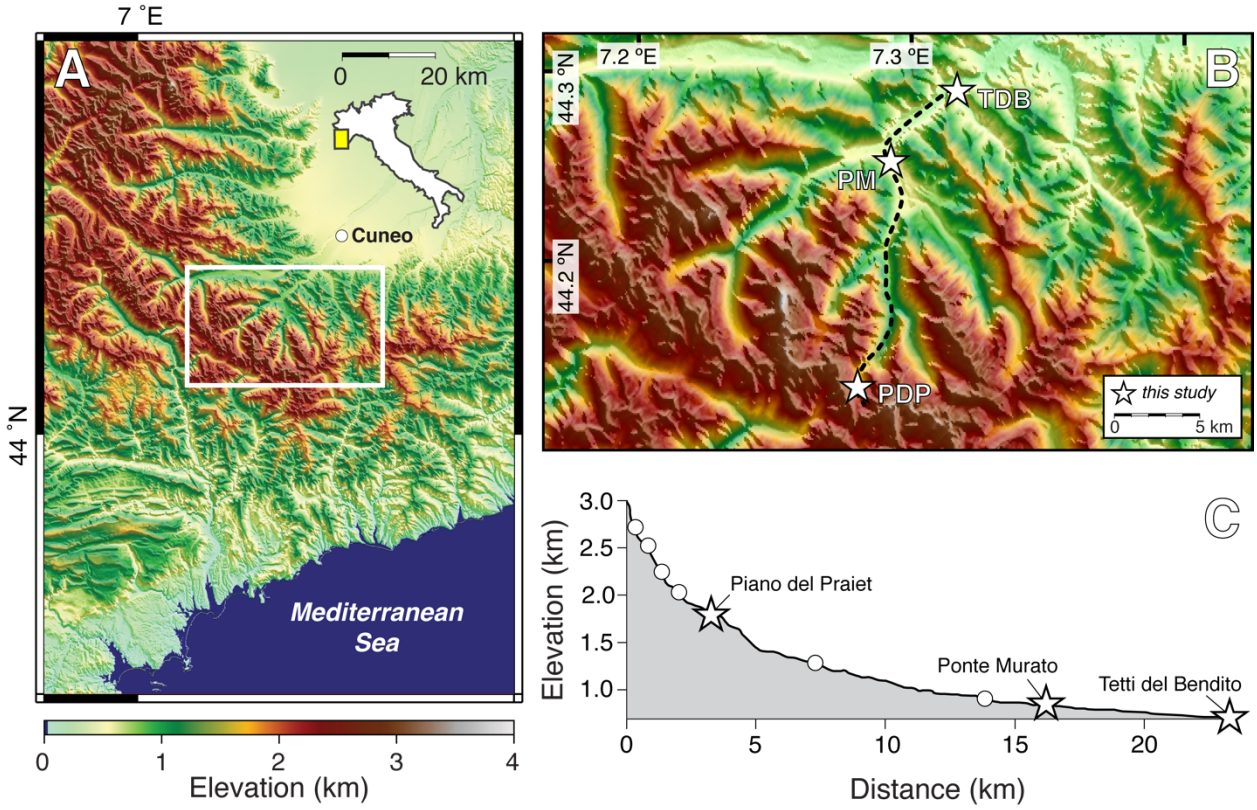

Figure 2: Grain size analysis for Gesso Valley samples. Histograms and solid curves denote the distribution of spherical equivalent radii for representative quartz grains (≥100) from the sieve fraction analyzed for cosmogenic ^{3}He abundances. Dashed curves denote the distribution of spherical equivalent radii in whole rock, inverted from the distribution of sectional circles of quartz

994 grains (≥100) measured in thin section. Thin sections were made from the same sample as the
995 crushed fraction, in the case of PDP10, or from a resampled boulder on the same moraine, in all
996 other cases. Vertical black lines denote the spherical equivalent radius of the single quartz grain
997 analyzed in each diffusion experiment shown in Fig. 4. For interpretation of references to color in
998 this figure, refer to the web version of this article.

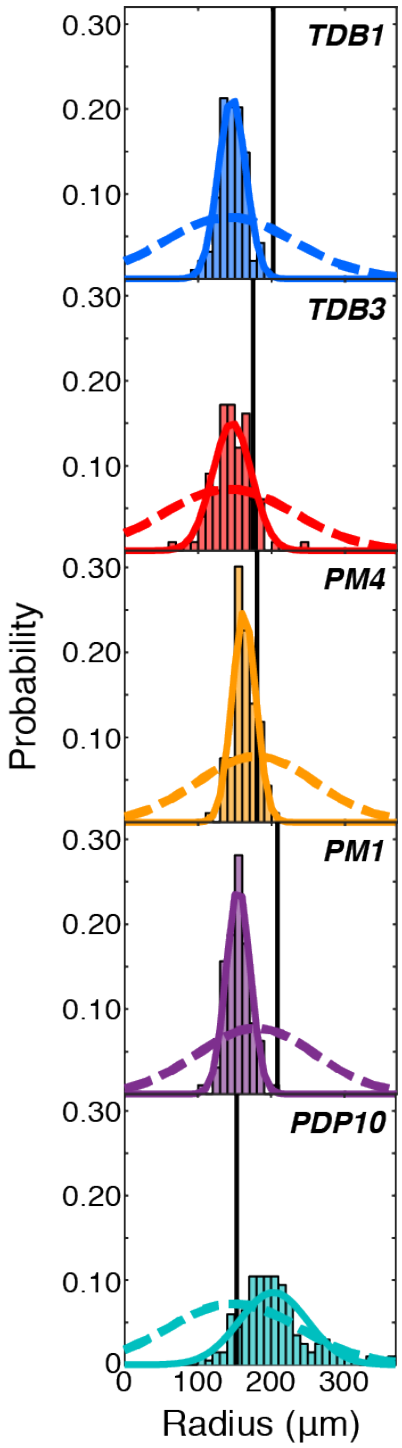
TDB1
TDB3
PM4
PM1
PDP10
0.30
0.20
0.10
0
Probability
0
100
200
300
Radius (µm)

999

Figure 3: Cosmogenic ^{3}He retention as a function of ^{10}Be exposure age in quartz from Gesso Valley moraine samples. Ellipses represent 1σ uncertainty. For interpretation of references to color in this figure, refer to the web version of this article.

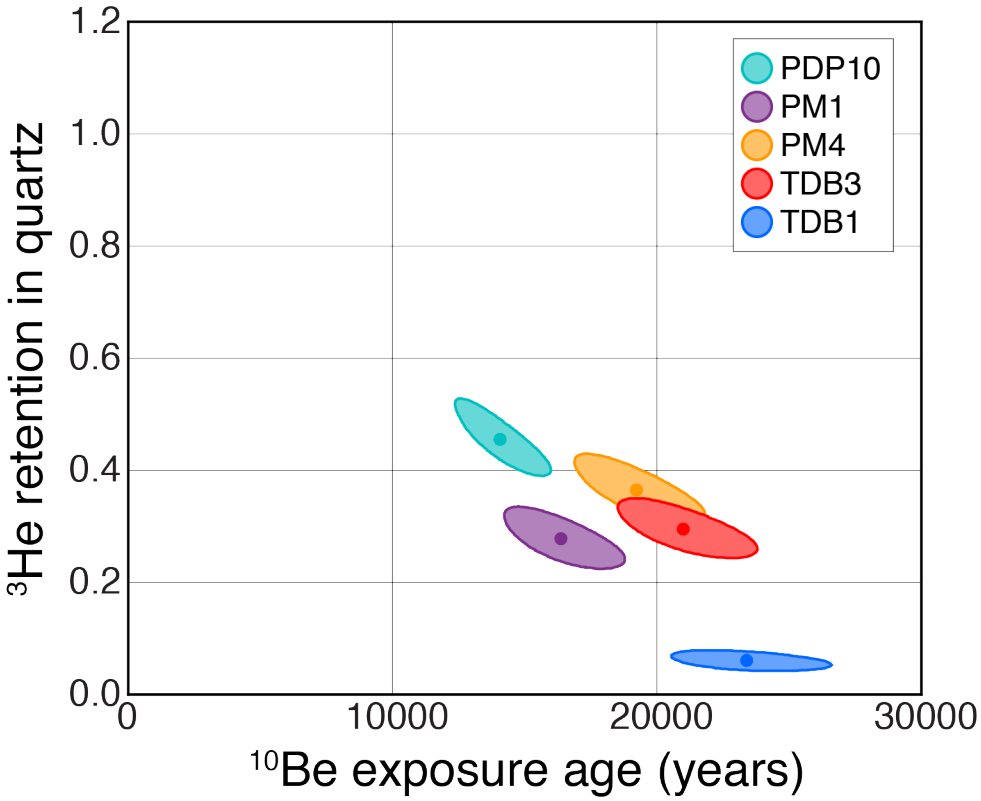

Figure 4: Arrhenius plots for helium diffusion experiments on Gesso Valley quartz samples. D/a^2 values are normalized to s^{-1}. Experimental data are plotted as gray circles. Diffusivities were calculated using the equations of Fechtig and Kalbitzer (1966) and the uncertainty propagation outlined in Tremblay et al. (2014b). Color circles and lines denote three-domain multiple diffusion domain (MDD) models that minimize misfit with the experimental data. Tremblay et al. (2017)

describe MDD modeling approach used here. For interpretation of references to color in this figure, refer to the web version of this article.

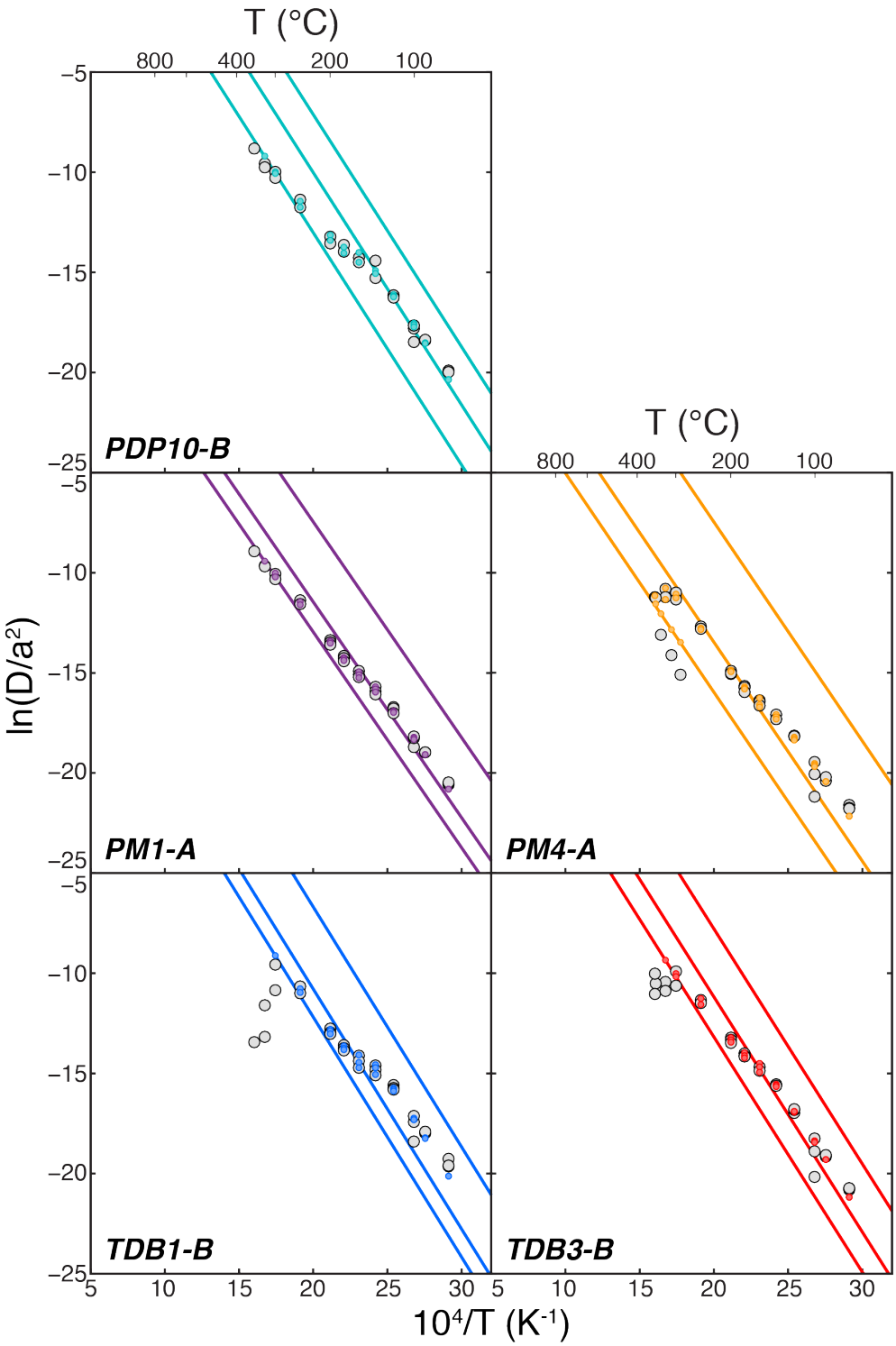

1012

Figure 5: Minimized misfit between observed and MDD-modeled ^{3}He diffusivities as a function of number of diffusion domains for Gesso Valley quartz samples. We increased the number of diffusion domains in our MDD models until the addition of another diffusion domain did not significantly reduce the misfit between the observed and calculated diffusivities. For all Gesso Valley quartz samples, we found that increasing the number of domains from three to four only marginally improved the misfit; therefore we use three-domain MDD models in subsequent calculations. For experiment PM1-A, attempts at constructing a four domain model yielded two domains with the same pre-exponential factor and thus are the equivalent of the three domain model. For interpretation of references to color in this figure, refer to the web version of this article.

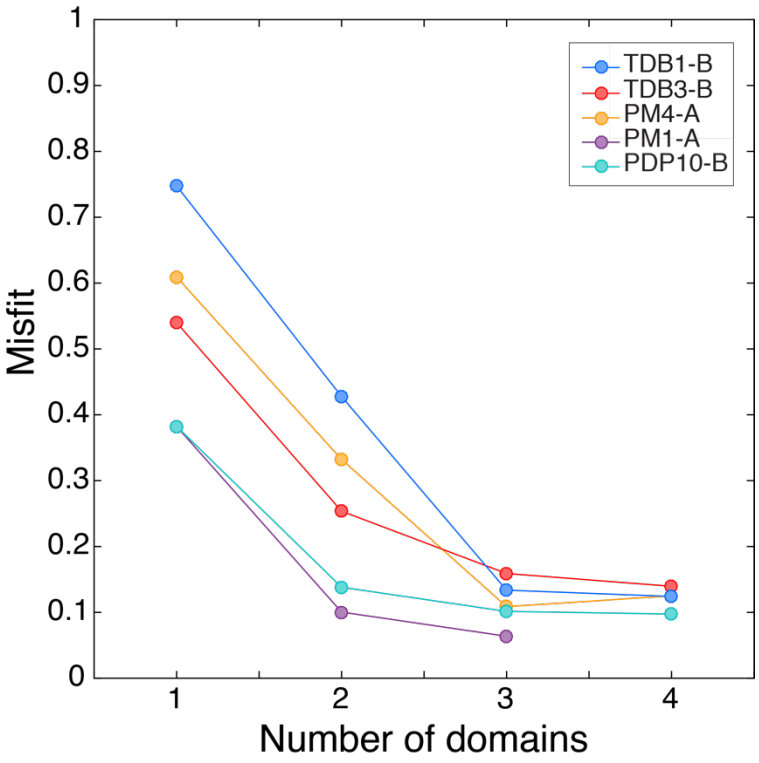

Figure 6: EDTs integrated over the exposure duration of Gesso Valley moraine samples. For each sample, we plot cosmogenic ^{3}He retention as a function of exposure duration for constant EDTs ranging from 0 to 30 ºC in 2 ºC increments, and assuming the MDD model diffusion kinetics reported in Table 3. Observed cosmogenic ^{3}He retention ellipses are plotted as in Fig. 4 for comparison. One set of EDT uncertainties in parentheses accounts for the uncertainty in ^{3}He retention and exposure duration as determined from ^{10}Be measurements; the second set of uncertainties accounts for uncertainty in the spherical equivalent radius to which the experimentally-determined diffusion kinetics are scaled in addition to the uncertainties in ^{3}He retention and exposure duration. For interpretation of references to color in this figure, refer to the web version of this article.

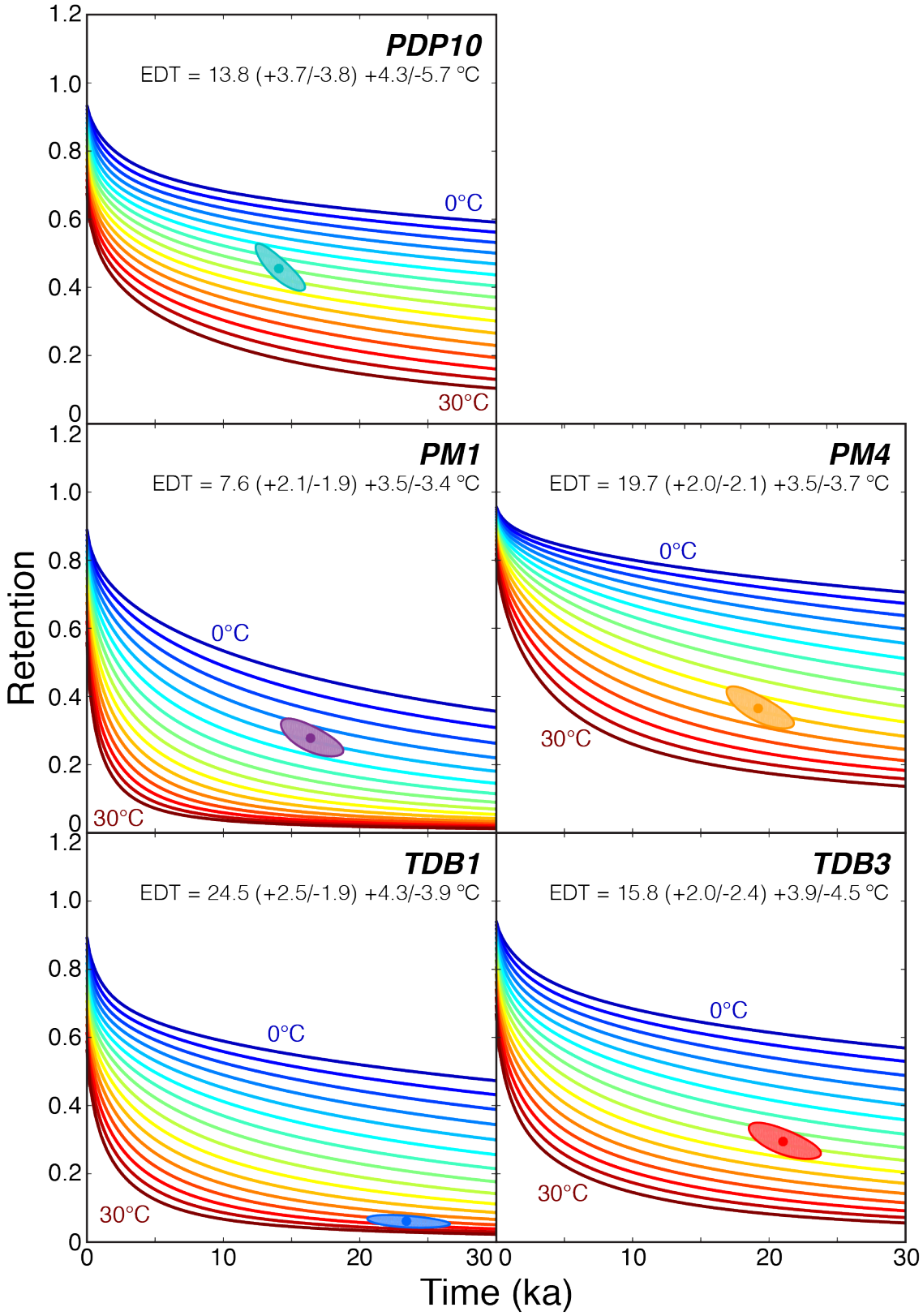
PDP10
EDT = 13.8 (+3.7/-3.8) +4.3/-5.7 °C
PM1
EDT = 7.6 (+2.1/-1.9) +3.5/-3.4 °C
PM4
EDT = 19.7 (+2.0/-2.1) +3.5/-3.7 °C
TDB1
EDT = 24.5 (+2.5/-1.9) +4.3/-3.9 °C
TDB3
EDT = 15.8 (+2.0/-2.4) +3.9/-4.5 °C
0°C
30°C
Retention
Time (ka)
0
0.2
0.4
0.6
0.8
1.0
1.2
0
10
20
30

Figure 7: EDTs calculated from modern meteorological data. In gray we show the time series of mean, minimum, and maximum daily temperatures from 2002 to mid-2016 at the elevations of the PDP, PM, and TDB moraines, scaled from the nearest two meteorological stations using average monthly lapse rates. Solid black bars denote the mean temperature for each time series; dashed black bars denote the modern EDT for each time series calculated using the activation energies of the best fit MDD models in Fig. 4 and Table 4. EDTs integrated over the exposure duration of each sample are also shown for comparison as circles, with colors for specific samples and 1σ uncertainties as reported in Fig. 6. For interpretation of references to color in this figure, refer to the web version of this article.

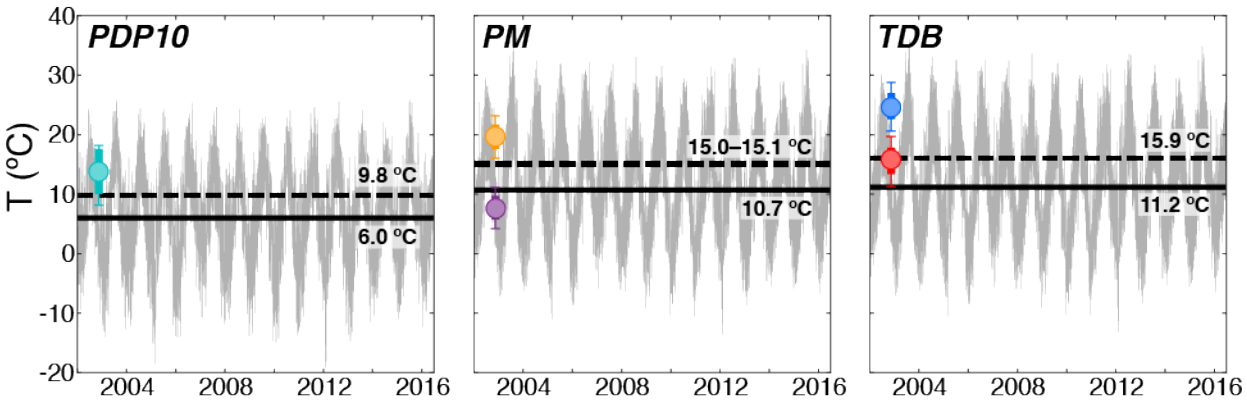

Figure 8: Cosmogenic ^{3}He retention in PDP10 quartz calculated from scaled TraCE-21ka seasonal temperatures and scaled, spliced chironomid July temperatures. The left panel shows the mean (black) and maximum (gray) seasonal temperature from the TraCE-21ka climate simulation and the mean July temperature (blue) from four spliced chironomid records, scaled to the elevation of PDP10 using modern lapse rate data and, for the chironomid records, weighted by distance from

1049 our study site. The right panel shows the evolution of ^{3}He retention with time assuming the TraCE-
1050 21ka and chironomid temperatures represent the EDT experience over PDP10's exposure duration.
1051 Thick retention curves assume the mean exposure duration and grain size for diffusion kinetics
1052 scaling; lower thin retention curves assume the +1σ exposure duration and grain size, while upper
1053 thin curves assume the –1σ exposure duration and grain size. The ellipse shows the observed
1054 retention and exposure duration, as in Fig. 3. For interpretation of references to color in this figure,
1055 refer to the web version of this article.

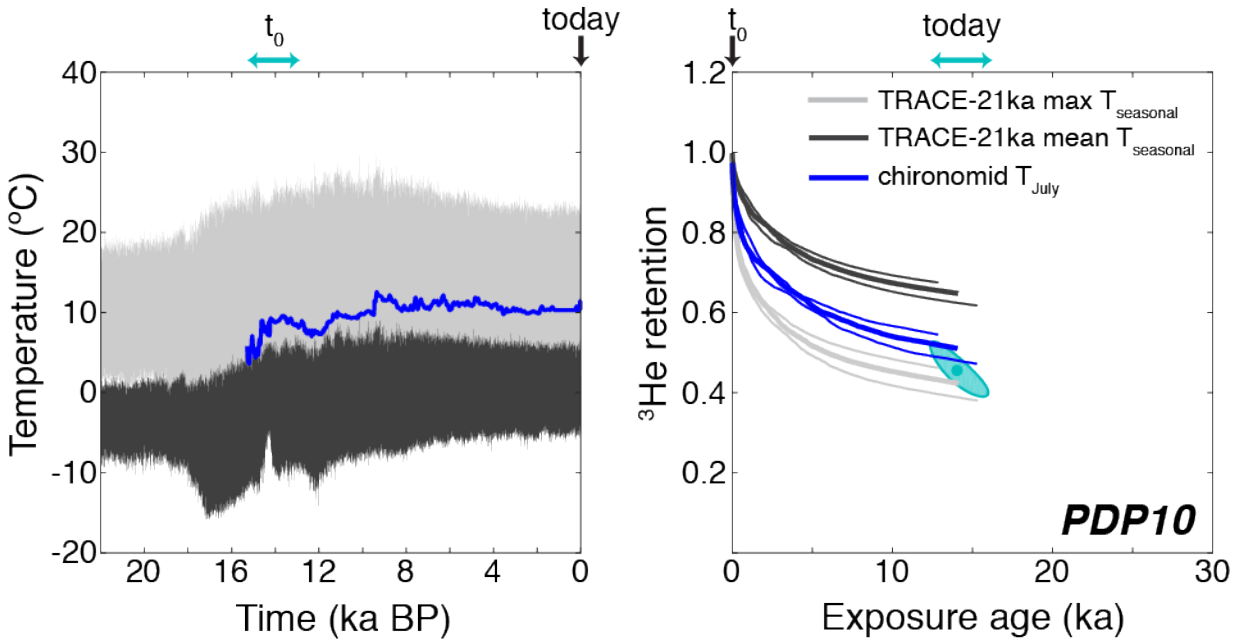

1056
1057
1058 **Figure 9:** Cosmogenic ^{3}He retention in PM1 and PM4 calculated from scaled TraCE-21ka
1059 seasonal temperatures and, in the case of PM1, scaled, spliced chironomid July temperatures. The
1060 left panel shows the mean (black) and maximum (gray) seasonal temperature from the TraCE-
1061 21ka climate simulation and the mean July temperature (blue) from four spliced chironomid

records, scaled to the elevation of PM using modern lapse rate data and, for the chironomid records, weighted by distance from our study site. The right panels show the evolution of ^{3}He retention with time assuming the TraCE-21ka and chironomid temperatures represent the EDT experience over the PM samples' exposure duration. Thick and thin retention curves are as in Fig. 8. Ellipses show the observed retention and exposure duration, as in Fig. 3. For interpretation of references to color in this figure, refer to the web version of this article.

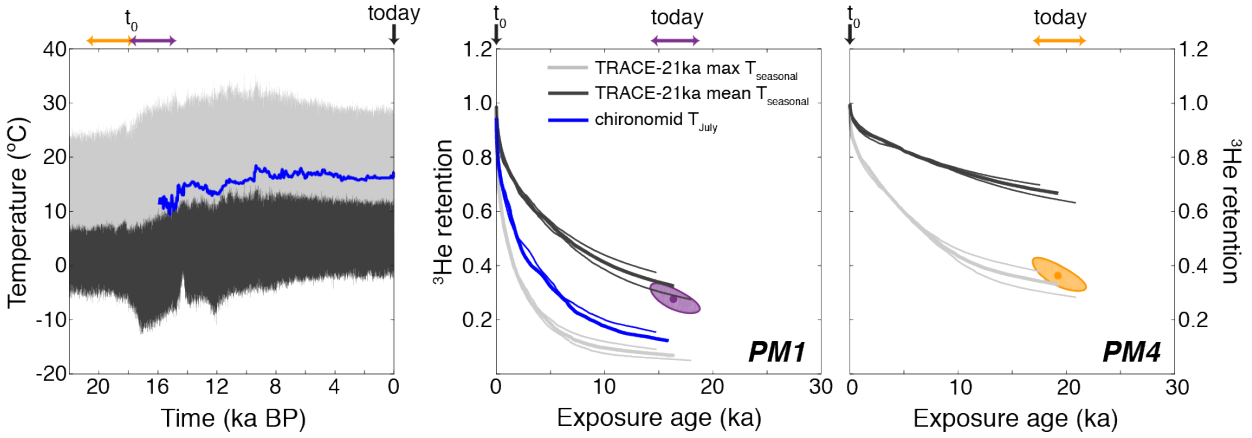

Figure 10: Cosmogenic ^{3}He retention calculated in TDB1 and TDB3 from scaled TraCE-21ka seasonal temperatures. The left panel shows the mean and maximum seasonal temperature from the TraCE-21ka climate simulation, scaled to the elevation of the TDB moraine using modern lapse rate data. The right panels shows the evolution of ^{3}He retention with time assuming the TraCE-21ka temperatures represent the EDT experience over the TDB samples' exposure duration. Thick and thin retention curves are as in Fig. 8. Ellipses show the observed retention and exposure

duration, as in Fig. 3. For interpretation of references to color in this figure, refer to the web version of this article.

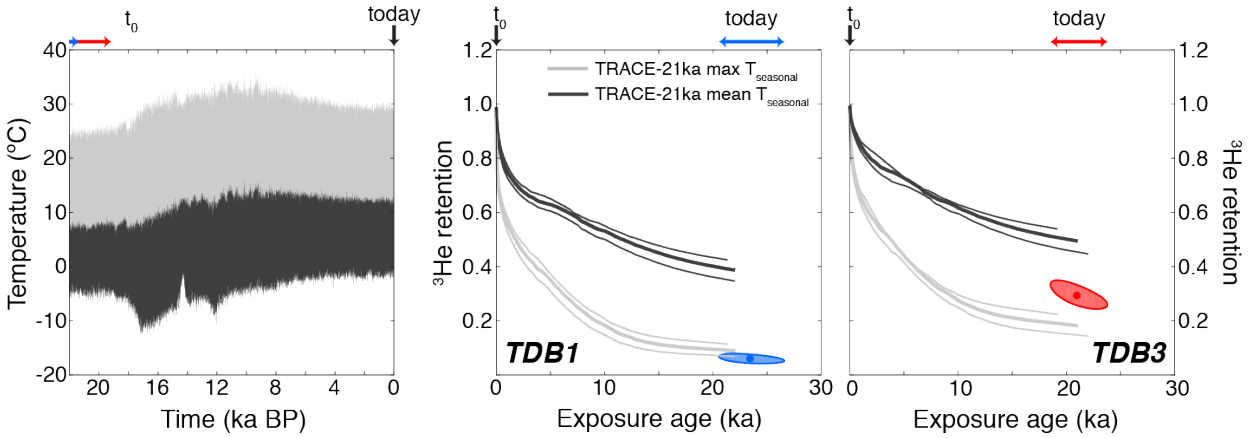

Figure 11: Minimized misfit between observed and MDD-modeled ^{3}He diffusivities as a function of activation energy E_a for Gesso Valley quartz samples, assuming a three domain diffusion model. Pre-exponential factors and gas fractions for each domain covary with E_a; we show misfit as a function of E_a because it is assumed to be common to all diffusion domains in our modeling approach. For interpretation of references to color in this figure, refer to the web version of this article.

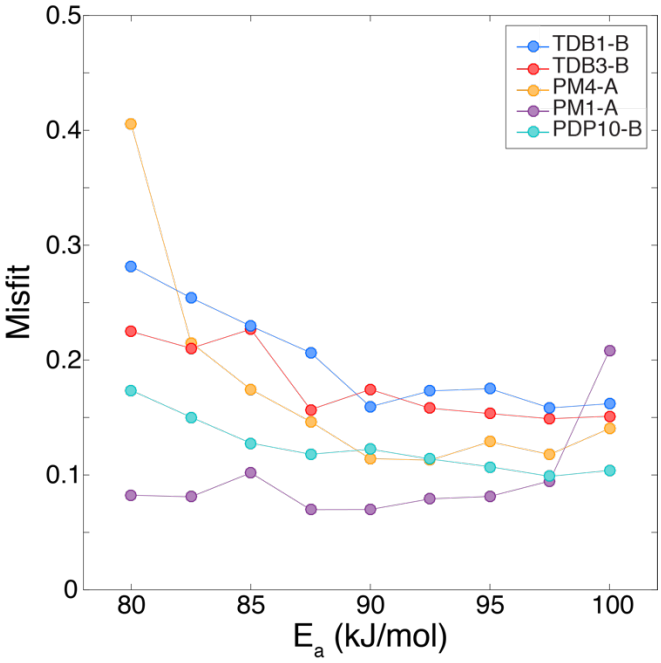
0.5
0.4
0.3
0.2
0.1
0
Misfit
80
85
90
95
100
E_a (kJ/mol)
TDB1-B
TDB3-B
PM4-A
PM1-A
PDP10-B

1086